1 2 3	Greenhouse Gas-Induced Modification of Intense Storms over the West African Sahel through Thermodynamic and Dynamic Processes
4	
5	
6	Siyu Zhao ¹ , Kerry H. Cook ¹ , Edward K. Vizy ¹
7	
8	¹ Department of Geological Sciences, University of Texas at Austin, Austin, TX, USA
9	
10	
11	Published in Climate Dynamics
12	
13 14 15	This preprint has not undergone any post-submission improvements or corrections. The Version of Record of this article is published in Climate Dynamics, and is available online at https://doi.org/10.1007/s00382-024-07193-3
16	
17 18	The citation for this work is as follows:
19 20 21 22 23	Zhao S, Cook KH, Vizy EK (2024) Greenhouse gas-induced modification of intense storms over the West African Sahel through thermodynamic and dynamic processes. Clim Dyn. https://doi.org/10.1007/s00382-024-07193-3
24	
25	Corresponding author address: siyu_zhao@utexas.edu
26	

Abstract

27

28

29

30

31

32

33

34

35

36

37

38

39

40

41

42

43

44

45

46

47

48

Convective-permitting ensemble simulations are used to understand the roles of thermodynamic and dynamic processes in changing intense storms over the West African Sahel due to increases in atmospheric greenhouse gas concentrations. Ensemble simulations with 16 members represent recent August conditions during the height of the boreal summer monsoon season over the Sahel. They are compared with 5 Future-Warming ensemble simulations with increased greenhouse gas concentrations under the late-21st-century high-emission SSP5-8.5 scenario and initial/boundary conditions from the Current-Climate data plus the multi-model mean anomalies derived from CMIP6 experiments. The Current-Climate simulations reproduce observed precipitation and environmental conditions over the Sahel well. The frequency of heavy rainfall events with 24-hr rainfall >77 mm (the 99.9th percentile) increases by $\geq 38.2\%$ in the Future-Warming simulations. While the low- to mid-level vertical wind shear increases in the Future-Warming simulations, we find no significant correlations between the environmental shear strength and peak storm rain rates. In contrast, lower (middle) tropospheric moisture and temperature are correlated (anticorrelated) with peak rain rates and/or the maximum updraft velocity of intense events, consistent with significant correlations between the increased atmospheric instability and storm intensity. Thus, thermodynamic processes and not dynamical (shear-related) processes dominate the rainfall intensification over the Sahel in the simulations. Nevertheless, the enhanced shear strength is associated with larger rain-shield areas and propagation speeds of intense storms in Future-Warming. Wind shear strength is also correlated with pre-storm atmospheric instability, which grows less/more under strong/weak shear with greenhouse gas increases and is relevant for sub/super Clausius-Clapeyron scaling of precipitation.

49

- 50 **Keywords**
- 51 Extreme precipitation, rainfall intensification, vertical wind shear, West African Sahel, climate
- 52 change, convective-permitting modeling

1 Introduction

53

54

55

56

57

58

59

60

61

62

63

64

65

66

67

68

69

70

71

72

73

74

The West African Sahel is vulnerable to floods during the boreal summer with the frequent occurrence of intense storms (Di Baldassarre et al. 2010). The mid-level African easterly jet (AEJ; Cook 1999) and the low-level southwesterly monsoonal flow (Hagos and Cook 2007; Cook and Vizy 2019) produce strong vertical wind shear across the Sahel that is observed and projected to increase as the amplified greenhouse gas-induced Sahara warming continues (Cook and Vizy 2015; Vizy and Cook 2017). Differences in the vertical wind shear and thermodynamic conditions associated with global warming may impact storms over the Sahel (Taylor et al. 2017; Bickle et al. 2020; Fitzpatrick et al. 2020). The purpose of our study is to understand the individual roles of thermodynamic and dynamic processes in modifying intense precipitation over the West African Sahel. Convectivepermitting (CP) ensemble simulations are used to represent the current and the late-21st-century August climatology over northern Africa. Compared to models with cumulus parameterization, CP modeling more realistically represents the mesoscale convective systems (MCSs) (Prein et al. 2015; Zhang et al. 2016a; Vizy and Cook 2018, 2019, 2023; Finney et al. 2019) that account for almost all of the heavy rainfall events over this region (Vizy and Cook 2022). Thus, this approach is needed for studying the processes responsible for future changes in intense storms across the Sahel. Section 2 reviews studies of greenhouse gas-induced thermodynamic and dynamic contributions to storm intensification as well as background on precipitation and environmental conditions over the Sahel. Section 3 describes the datasets, analysis methods, and experimental

design. Results are discussed in Section 4, and conclusions are summarized in Section 5.

2 Background

There are ongoing efforts to physically understand how heavy precipitation in the tropics responds to increasing greenhouse gas levels. The thermodynamic contribution to the storms' response to global warming is better understood than other mechanisms (Shepherd 2014; Trenberth et al. 2015; Pfahl et al. 2017). Assuming rainfall scales with lower-tropospheric moisture, the thermodynamic contribution is often approximated by or compared to the Clausius-Clapeyron (CC) scaling that predicts a 6-7% increase in rainfall intensity for each 1 K increase in surface temperature (Seneviratne et al. 2021; Trenberth et al. 2003).

Some studies report that the observed trends of extreme precipitation over the U.S. and the globe generally follow the CC scaling (Westra et al. 2013; Fischer and Knutti 2016; Barbero et al. 2017; Sun et al. 2021) There are some regions showing super- (sub-) CC scaling of rainfall extremes in observations or model simulations (Sugiyama et al. 2010; Lenderink et al. 2017, 2021; Neelin et al. 2022). One potential reason for the super- (sub-) CC scaling is changes in atmospheric instability with global warming. Larger CAPE values or atmospheric conditions with larger temperature or moisture vertical gradient are linked to higher rainfall intensity in idealized squall-line simulations (Takemi 2006, 2007a, b, 2014). Using a simple entraining plume model, Loriaux et al. (2013) find that the scaling of intense rainfall decreases from super-CC to CC when atmospheric stability is increased in the future simulation with temperature perturbations to the current simulation adjusted from constant to moist adiabatic increase across height.

Dynamical feedbacks that increase moisture convergence for storms are proposed as important processes for super-CC scaling of extreme precipitation (Haerter and Schlemmer 2018; Lochbihler et al. 2021; Neelin et al. 2022). As one relevant environmental factor, low-tropospheric shear of a suitable magnitude and a direction perpendicular to the squall line is posited to enhance

convective/rainfall intensity and duration (Weisman et al. 1988; Rotunno et al. 1988; Weisman and Rotunno 2004). Shear strength is suggested to be optimal for storm development when it balances the vorticity of the storm's cold pool and is the most favorable for maintaining the vertical position of the storm's updraft and triggering deep convective cells at the storm's edge. Some studies (Takemi 2006, 2007a) support this theory, while others (Stensrud et al. 2005; Coniglio et al. 2012) question its applicability in observations and suggest the prevalence of deep-layer shear during the development of intense storms. Some studies show that strong vertical wind shear at mid- or upper levels suppresses convective and/or rainfall intensity of storms (Wang and Prinn 1998; Chen et al. 2015). Alfaro and Khairoutdinov (2015) and Alfaro (2017) put forth an alternative theory that strong low-tropospheric shear favors high squall-line intensity primarily through increasing convectively unstable air in the total storm-relative inflow and enhancing the storm's latent heating rather than interacting with the storm's cold pool.

Our study focuses on the response of intense storms to greenhouse gas forcing over the West African Sahel. This region is known for frequent occurrence of intense storms and catastrophic floods that results in economic losses and the loss of lives (Di Baldassarre et al. 2010). MCSs produce 70-95% of the total rainfall (Laurent et al. 1998; Laing et al. 1999; Mathon et al. 2002; Mohr 2004; Liu et al. 2019) and almost all of the heavy rainfall events (Vizy and Cook 2022) over the West African Sahel during the boreal summer monsoon season (Hagos and Cook 2007; Cook and Vizy 2019). Climate models with cumulus parameterizations have limited ability to reproduce MCS evolution and rainfall diurnal cycles over this region (Rossow et al. 2013; Zhang et al. 2016a, b), suggesting deficiency in their ability to simulate extreme rainfall events.

The West African Sahel exhibits a unique thermodynamic and dynamic environment for storm development in the boreal summer compared with other tropical regions. The moist lowlevel monsoon flow from the Gulf of Guinea converges with dry Saharan air over the Sahel, forming a dryline boundary (Eldridge 1957) and a capping inversion that favors instability build-up and genesis of intense storms (Vizy and Cook 2018, 2019, 2022). Vertical wind shear is strong across the Sahel as the low-level southwesterly monsoonal flow lies below the mid-tropospheric African easterly jet (AEJ; ~15°N, 600 hPa). The AEJ is geostrophically forced by the surface/low-level temperature gradients between the Sahara and equatorial Africa (Cook 1999). The strength of the AEJ is related to the magnitude of the warming over the Sahara during the boreal summer (Lavaysse et al. 2010; Cook and Vizy 2015; Lavaysse 2015; Vizy and Cook 2017).

Precipitation trends over the West African Sahel in recent decades show increased intensity and frequency of intense rainfall, which are associated with greenhouse-gas forcing and the Sahel's rainfall recovery since the 1980s (Dong and Sutton 2015; Taylor et al. 2017; Bichet and Diedhiou 2018; Panthou et al. 2018; Chagnaud et al. 2022). Further increases in heavy rainfall intensity are predicted over the West African Sahel by climate models with or without cumulus parameterization (Berthou et al. 2019; Dosio et al. 2019, 2020; Kendon et al. 2019).

Storm intensification over the West African Sahel has been associated with differences in both the thermodynamic and dynamic environment. The precipitable water, CAPE, and CIN are expected to increase over the West African Sahel with climate change (Bickle et al. 2020; Fitzpatrick et al. 2020). In addition, the Sahara is observed and projected to experience amplified warming (Cook and Vizy 2015; Vizy and Cook 2017), which increases meridional temperature gradients across the Sahel, strengthening the AEJ and the vertical wind shear (Patricola and Cook 2010, 2011; Skinner and Diffenbaugh 2014; Kebe et al. 2020). Although one study projects a weakening of the AEJ with greenhouse gas increases using a different model and analysis period from other simulations (Bercos-Hickey and Patricola 2021), ECMWF Re-Analysis 5 (ERA5;

Hersbach et al. 2020) indicates an observed positive trend of ~0.03 m s⁻¹ yr⁻¹ in the 600-hPa AEJ wind speed over the West African Sahel during August from 1979 to 2020.

The relative importance of thermodynamic and dynamic processes for storm intensification over the West African Sahel is not fully understood. Taylor et al. (2017) suggest that enhanced shear and mid-level drying are the primary mechanisms for the observed MCS intensification over the Sahel since the 1980s. Baidu et al. (2022) observe that storms have colder brightness temperatures at the cloud top and higher surface rain rates with stronger vertical wind shear over West and Central Africa. Using a CP climate model at 4.5 km resolution, Fitzpatrick et al. (2020) find that pre-storm vertical wind shear is associated with in-storm vertical velocity and cloud-top temperatures of storms but it is not directly correlated with surface rain rates. They suggest that higher precipitable water is the primary driver for the heavier rainfall over the Sahel with global warming. Bickle et al. (2020), using idealized simulations initialized with atmospheric conditions representative of the West African Sahel, find that thermodynamic processes are more important for storm intensification over the Sahel than enhanced shear.

Further research is required to evaluate the thermodynamic and dynamic contributions to the change in heavy rainfall with greenhouse gas increases over the West African Sahel. Our study improves this understanding by conducting physical analysis for storms over the Sahel region using 3-km CP ensemble simulations and available state-of-the-art reanalysis/observations.

3 Methodology

a. Datasets and Analysis Methods

The following datasets are used to evaluate and/or serve as initial/lateral/ocean surface boundary conditions for the regional CP simulations. The rainfall and reanalysis datasets have fine

spatial and temporal resolutions suitable for the study of storm development, especially over Africa with the lack of ground-based data (Dezfuli et al. 2017). The sea surface temperature (SST) dataset realistically represents conditions over the oceans adjacent to or inland water bodies over Africa (Argent et al. 2015; Liu et al. 2020). The datasets are:

- NASA Integrated Multi-satellitE Retrievals for GPM (IMERG; Huffman et al. 2019):

 IMERG is a 0.1° half-hourly dataset from 2000 to present.
- ECMWF Re-Analysis 5 (ERA5; Hersbach et al. 2020): ERA5 is a 0.25° hourly reanalysis from 1979 to present.
 - UK Met Office Operational Sea-surface Temperature and Ice Analysis (OSTIA; Donlon et al. 2012): OSTIA is a 0.054° daily dataset from 2006 to present.

We select heavy rainfall events that produce the highest 24-hr rainfall totals over the West African Sahel, following the method of Vizy and Cook (2022). First, 12Z-12Z (UTC) precipitation totals for all grid points are ranked in the analysis region (12°N-18°N, 9°W-20°E; Figure 1) that avoids the coast and the Marrah Mountains (~13°N, 24°E). The 12Z-12Z time window accommodates typical diurnal rainfall peaks over the analysis region (Zhang et al. 2016b). Heavy rainfall events are then identified as events that produce 24-hr rainfall totals at the 99th percentile in the control simulation. This value is 77 mm of rain in 24 hr. Since MCSs often propagate across hundreds of kilometers, a distance threshold is applied to avoid double counting rainfall events. Events are excluded if they are located within 500 km of a grid point with a higher 24 h rainfall total within the same 12Z-12Z time period. This distance criterion is useful for selecting a representative population of heavy rainfall events. Tests using various distance (200, 300, and 700

km) do not change the results of the paper but indicate that the projected frequency increase of heavy rainfall events is a conservative estimate.

Several indices are developed to measure precipitation accumulation, rainfall/convective intensity, and storm characteristics of heavy rainfall events in a Eulerian framework (Table 1). Rainfall totals of each event are associated with both event duration and mean rainfall intensity, and the event duration is further related to the storm's rain-shield area and anti-correlated with the storm propagating speed (Doswell et al. 1996). Thus, indices are derived for rainfall totals, duration, and mean/peak rainfall intensity of the event, as well as (height of) the storm's maximum updraft velocity, rain-shield area, and propagating speed at the time of the peak rain rate. Figure 1 illustrates the method of deriving the storm's rain-shield area and propagating speed for an example event. Similar plots are examined for each event to ensure correct computation of storm indices. Additional information is given in Online Resource 1.

Multiple indices are developed to quantify the vertical wind shear and thermodynamic conditions prior to the heavy rainfall events (Table 2). The shear indices are computed between 600 hPa and 925 hPa, which are close to the peak amplitude of the mid-level AEJ and the low-level monsoonal flow over the West African Sahel. The moisture and temperature indices are computed at 800 hPa (600 hPa), which is representative of the lower (middle) tropospheric conditions across Sahel. Low-level CAPE/CIN is used to measure atmospheric instability together with vertical gradients of moisture/temperature and moist static energy (MSE) according to:

$$MSE = C_p T + \Phi + L_v q, \tag{1}$$

where T, Φ , and q represent temperature, geopotential, and specific humidity, respectively, C_p is the specific heat capacity of dry air at constant pressure (1004 J kg⁻¹ K⁻¹), and L_v is the latent heat of water vaporization (2.5×10⁶ J kg⁻¹).

b. Experimental design

National Center for Atmospheric Research (NCAR) Weather Research and Forecasting Model Version 4.1.3 (WRF; Skamarock et al. 2019) is used to run the CP simulations. Figure 2 presents the model configuration with 27/9/3-km triple nested domains using one-way nesting. The 27-km domain covers a large part of tropical and North Africa. Its lateral boundaries are set far from the West African Sahel to avoid strict constraints from the prescribed lateral boundary conditions. Each domain has 43 vertical levels, with the top of atmosphere set at 10 hPa.

Model output is written out every 3/3/1 hours for the 27/9/3-km domains, respectively. The hourly output from the 3-km domain is useful for studying precipitation and environmental conditions associated with storm development. To improve model stability, simulations in our study use an adaptive positive definite 6th order horizontal diffusion damping based on previous CP modeling research (Hutchinson 2009; Jeworrek et al. 2019). The diffusion coefficients for the 27/9/3-km domains are 0.2-0.25/0.3-0.35/0.3-0.4. An adaptive model time step is also applied in the 27/9/3-km domains, with time steps occasionally adjusted from 90/30/10 s to 45/15/5 s.

Cumulus parameterization is turned off in the 3-km domain, which simulates convection explicitly. The 27-km and 9-km domains utilize the Kain-Fritsch cumulus convective scheme (Kain 2004). Other physical parameterizations are the same for all three domains, including Thompson microphysics (Thompson et al. 2008), RRTM longwave radiation (Mlawer et al. 1997), Dudhia shortwave radiation (Dudhia 1989), Revised MM5 surface layer (Jiménez et al. 2012), Yonsei University planetary boundary layer (Hong et al. 2006) schemes and Unified Noah Land Surface Model (Chen and Dudhia 2001). Choices of these parameterizations are based on studies

that generate realistic simulations of African climate using regional models (Vizy and Cook 2009, 2018, 2019; Laing et al. 2012; Vizy et al. 2013; Crétat et al. 2015).

This study uses simulations from Zhao et al. (2022) as a Current-Climate experiment. The experiment includes 16 ensemble members, which capture present-day climate conditions over the West African Sahel. The model concentrations of CO₂, N₂O, and CH₄ are set as 379 ppmv, 319 ppbv, and 1774 ppbv, with the CO₂ concentration close to the observed value in 2005. Each simulation is run from 00Z 01 July to 00Z 01 September, with the first month devoted to model spin-up. August, the peak of the local rainy season, is chosen as the analysis period. The 3-hourly ocean boundary conditions for all ensemble members are derived from OSTIA 2007-2019 climatological SSTs that are smoothed with a 30-day running mean. The ensemble simulations suppress short-term SST variability on synoptic to interannual time scales, focused on the representation of climatological conditions over the West African Sahel. Thus, the simulations are not expected to reproduce weather of specific years but are evaluated against the climatological environmental conditions and rainfall distribution over the West African Sahel.

Initial, lateral boundary, land surface, and/or soil conditions are different in each of the Current-Climate ensemble members (Table 3). Initial and 3-hourly lateral boundary conditions are derived from the ERA5 reanalysis for years between 2013 and 2017. The ensemble members are further differentiated by the treatment of Lake Chad, which varies between a small lake and a large lake, with different treatments of the wetlands. Zhao et al. (2022) evaluated the regional effects of different lake configurations in these simulations. They found that the variations in the specification of Lake Chad do not impact the climate – including intense rainfall events - over the West African Sahel, making these simulations ideal as a control simulation for the current study.

The Future-Warming simulation includes 5 ensemble members, which is sufficient to establish statistically significant differences from the control simulation. We use an 'anomaly forcing' approach (e.g., Patricola and Cook 2010, Cook and Vizy 2012, Liu et al. 2017) to represent late-21st-century conditions under the Shared Socio-economic Pathways 5-8.5 (SSP585) scenario, which hypothesizes fossil-fueled development (O'Neill et al. 2016; Chen et al. 2021). Concentrations of CO₂, N₂O, and CH₄ are increased to 940 ppmv, 384 ppbv, and 2581 ppbv, respectively, which are the projected 2071-2100 global annual mean concentrations in SSP585. Initial and boundary conditions for the Future-Warming ensemble members are the Current-Climate data plus multi-model mean future anomalies from CMIP6 simulations (Eyring et al. 2016). To derive these anomalies, differences are computed between CMIP6 SSP585 monthly mean simulation output averaged over 2071-2100 and historical experiment output averaged over 1985-2014 for five coupled general climate models (CGCMs). The differences are averaged and interpolated to 3-hourly values in the ERA5 or OSTIA grid, and added to the regional model's lateral or SST boundary conditions.

The future anomalies are derived from multiple CMIP6 models (Table 4) to avoid reliance on climate projections from a single model. The choice of the CMIP6 models is based on the models' performance in realistically simulating the current African climate (Iyakaremye et al. 2021; Klutse et al. 2021; Quenum et al. 2021; Makinde et al. 2022; Mwanthi et al. 2022) and a likely range of global mean SST increase (2.01-4.07 K) from 1995-2014 to 2081-2100 in SSP585 (Fox-Kemper et al. 2021). The variables adjusted in the initial and lateral/surface boundary conditions include geopotential, temperature, horizontal wind, relative humidity, surface pressure, mean sea level pressure, skin temperature, and SSTs. Figure 2 shows the August mean SST differences between the Future-warming and Current-Climate experiments. SST warming greater than 2.5 K

is predicted over the eastern equatorial Atlantic and over the open ocean away from the northern African coast. SST anomalies are set to 3 K over African inland waters and the Red Sea, and 4.35 K over the Mediterranean Sea, based on representative values derived from CMIP6 simulations.

The 'anomaly forcing' approach differs from a direct downscaling of CGCM output since it only uses projected anomalies from CGCMs and uses a large domain to minimize influence from the anomalies applied on the lateral boundaries. SST anomalies are the primary influence from the CGCMs in the Future-Climate simulation, and the Current-Climate simulation is completely independent of the CGCMs. This method limits introducing errors from individual CGCMs into the regional model domain, and has been proved useful for studying climate change over Africa in previous studies (Patricola and Cook 2010, 2011, 2013a, b; Cook and Vizy 2012; Vizy and Cook 2012; Vizy et al. 2013).

4 Results

a. Evaluation of the Current-Climate Experiment

Figure 3a shows the August mean precipitation from IMERG for the 2000-2019 climatology. There is sharp meridional precipitation gradient across the analysis region with magnitudes decreasing from around 7 mm day⁻¹ at 12°N to less than 1 mm day⁻¹ by 18°N. Rainfall rates are higher south of 12°N, with local maxima of ~10 mm day⁻¹ present over Guinea Highlands (~10°N, 10°W), the Cameroon Highlands (~7°N, 11°E), and the Jos Plateau (~10°N, 9°E).

Figure 3b presents the ensemble mean rainfall in the 3-km domain of Current-Climate. The simulations capture the meridional rainfall gradient over the Sahel and precipitation maxima over the topography of tropical Africa. These patterns agree well with IMERG. The simulated rainfall

amounts are ~1 mm day⁻¹ lower than IMERG over tropical Africa and the northern part of the analysis region (15°N-18°N, 0-20°E). This difference falls within the uncertainty of IMERG.

Figure 3c illustrates the exceedance probability of 12Z-12Z 24-hr August rainfall totals at the grid point over the analysis region from 20 years of the IMERG record (2000 – 2019) and 16 Current-Climate ensemble simulations. In general, the Current-Climate ensemble reproduces the observed frequency distribution of 24-hr precipitation over the analysis region, with the 99th (99.9th) percentile of 49 (89) mm in IMERG and 42 (77) mm in Current-Climate. The frequency curve of Current-Climate lies below than that of IMERG. This is associated with drier conditions over the northern part of the analysis region in Current-Climate than in IMERG (Figs. 3a-b).

Figure 4a shows the spatial distribution of heavy rainfall events that produce 24-hr rainfall totals greater than 77 mm at a grid point in the analysis region in IMERG. 77 mm is the 99.9th percentile of 24-hr precipitation in Current-Climate (Fig. 3c). 90.1% of the heavy rainfall events are associated with 24-hr rainfall totals below 150 mm, and the wettest event generates 280 mm precipitation; 87.0% of the events are located south of 15°N. The most extreme events with 24-hr rainfall totals above 150 mm occur in several clusters, including over southwestern Mali (~12°N, 8°W), north of the Jos Plateau (~12°N, 8°E), near Lake Chad (~13°N, 12°E), and over central Chad (~13°N, 18°E). These results are generally consistent with Vizy and Cook (2022). There is some uncertainty in the cluster over the Lake Chad because IMERG may overestimate precipitation over inland water bodies (Tian and Peters-Lidard 2007; Taylor et al. 2018).

The spatial distribution of heavy rainfall events in Current-Climate (Fig. 4b) is generally similar to that in IMERG south of 15°N and west of Lake Chad. Elsewhere, Current-Climate does not simulate clusters of heavy rainfall events over Lake Chad and eastern Chad (~12°N, 20°E), or intense precipitation over central Niger and Chad (16°N-18°N, 5°E-15°E).

Figure 4c shows the number of heavy rainfall events in August over the analysis region from IMERG and Current-Climate, while the inset shows a closer view of upper end of the distribution curves greater than 150 mm. The thick lines denote the 20-yr IMERG mean or the simulation ensemble mean. The thin lines represent data for the individual years/ensemble members to quantify their range. The frequency distributions and interannual/ensemble member variability of heavy rainfall events are similar between Current-Climate and IMERG. The most extreme event in Current-Climate produces 334 mm 24-hr rainfall totals, higher than that in IMERG. Current-Climate also shows a higher frequency of rainfall events with 24-hr precipitation totals between 77 and 150 mm than IMERG.

To evaluate the environmental conditions in which storms develop over West Africa, Figure 5a shows the climatological August specific humidity and horizontal winds at 925 hPa from ERA5. 925 hPa is representative of lower tropospheric conditions from the surface to 850 hPa. At low levels there is a sharp meridional gradient in atmospheric moisture across the West African Sahel. Specific humidity values are relatively high (~15 g kg⁻¹) near and south of 12°N over tropical Africa, but decrease to around 9 g kg⁻¹ by 18°N. Southwesterly monsoonal flow from the Guinean coast penetrates into the analysis region and converges with northerlies from the Sahara.

Figure 5b shows the ERA5 August specific humidity and horizontal winds at 600 hPa, a representative mid-tropospheric layer. At this level the highest specific humidity values (5.5 g kg⁻¹) occur over tropical Central Africa (~5°N-12°N, 10°E-30°E) and decrease northward, but not as sharply as at 925 hPa. The AEJ overlays the low-level southwesterlies, producing strong vertical wind shear with the maximum 925 hPa – 600 hPa wind difference of ~18 m s⁻¹ centered around 15°N in the ERA5 August climatology (Fig. 5c).

Figures 5d-f are similar to Figs. 5a-c but for the Current-Climate simulations. Current-Climate generally reproduces ERA5's August moisture and circulation patterns over northern and tropical Africa. The low-level meridional moisture gradient in Current-Climate is positioned about 2° of latitude further south than in ERA5, the low-level (Fig. 5d) environment is generally drier across the Sahel in Current-Climate by ~2.6 g kg⁻¹. At mid-level (Fig. 5e), the northerly component of the AEJ is stronger in Current-Climate, while the simulated maximum 925 hPa – 600 hPa wind difference is ~1.4 m s⁻¹ lower over the Sahel compared to ERA5 (Fig. 5f). The drier low- and mid-level environment is consistent with the low number of simulated heavy rainfall events across the northern Sahel compared to IMERG (Fig. 3) - 83.9% of the observed events north of 15°N are associated with totals less than 125 mm. Most of the heaviest events in the analysis region occur south of 15°N and Current-Climate simulations realistically represent this population of storms.

In conclusion, the spatial and frequency distribution of (intense) rainfall from Current-Climate generally agrees with IMERG. The simulations also realistically represent environmental conditions including the low to mid-level moisture and circulation patterns over the north and tropical Africa during the height of the summer monsoon season (August) compared with ERA5. While there are some caveats as highlighted above, the Current-Climate simulations will be useful in understanding the evolution of intense storms over the West African Sahel.

b. Projections from the Future-Warming Experiment

Figure 6a shows the ensemble mean August precipitation from the Future-Warming experiment. The largest rainfall rates over western and central Africa occur between ~7°N-15°N, similar to Current-Climate (Fig. 3). Maxima with rates greater than 10 mm day⁻¹ occur near and south to 12°N over tropical Africa, and over the Cameroon Highlands.

Figure 6b shows August ensemble mean rainfall differences between Future-Warming and Current-Climate. Positive rainfall anomalies of around 2 mm day⁻¹ occur over much of the Sahel and parts of East Africa (2°N-15°N, 25°E-34°E), with the largest increase (~9 mm day⁻¹) occurring over the Marrah Mountains in Future-Warming compared to Current-Climate. South of the Sahel there is a significant decrease in precipitation over the Guinean Highlands, the Cameroon Highlands and tropical Central Africa (2°N-10°N, 15°E-25°E). The projections are consistent with a few other studies using models with or without cumulus parameterizations (Roehrig et al. 2013; Vizy et al. 2013; Maidment et al. 2015; Zhang and Li 2022; Berthou et al. 2019).

Figure 6c shows the exceedance probability of 12Z-12Z 24-hr August rainfall totals at a grid point over the analysis region from Future-Warming and Current-Climate, similar to Fig. 3c. The frequency curve derived from Future-Warming exhibits a flatter gradient than that from Current-Climate, indicating an increased probability of occurrence across all storm populations over the analysis region. The 99th (99.9th) percentile of 24-hr precipitation over the analysis region is 59 (104) mm in Future-Warming, 17 (27) mm higher than the Current-Climate values. In other words, an average grid point over the Sahel region in Future-Warming is 1.6/2.9 times more likely to have heavy (99th/99.9th) rainfall from the perspective of Current-Climate.

Figure 7a shows the spatial distribution of heavy rainfall events that generate 24-hr precipitation more than 77 mm at a grid point in the analysis region in Future-Warming. The spatial distribution of these heavy rainfall events is similar to that in Current-Climate (Fig. 4b), with 88.5% of the events located south of 15°N. The heaviest rainfall events cluster over southwestern Mali, Burkina Faso (~13°N, 2°W), and north of the Jos Plateau.

Figure 7b shows the frequency distribution of heavy rainfall events in August from Current-Climate and Future-Warming, with the inset magnifying the upper end of the distribution.

Events with 24-hr rainfall totals above 77 mm increase by ~20 events per month over the analysis region from Current-Climate to Future-Warming. The frequency increase of events between 77 and 175 mm in Future-Warming exceeds the range of ensemble member variability of Current-Climate as indicated by the clear separation between the thin lines of the two ensemble experiments. The frequency of events between 175 and 250 mm in Future-Warming is similar to that in the wettest ensemble members of Current-Climate, increasing from ~2 events per August in Current-Climate to ~9 events per August in Future-Warming. The highest event occurs in the Current-Climate experiment, but a larger number of ensemble members is required to investigate whether/how the frequency of rarest rainfall events (>250 mm) changes in the future.

The top 30 events with highest 24-hr precipitation are selected from each ensemble simulation, that is a total of 480 (150) events from Current-Climate (Future-Warming). Figure 8 shows the rainfall and storm characteristics of the selected events, which are sorted by their total precipitation, Ptotal (Table 1), on the x-axes. In Current-Climate, the average event duration, Dtotal, ranges from 4.4 to 6.5 hours (Fig. 8a) with rainfall events with longer durations more likely to generate higher rainfall totals at one location. The longer durations of the top-ranked events (1st – 20th) are associated with decreases in storm propagating speed, Vpeak (Fig. 8b), but they are not linked with variations in the storm's rain-shield area, Apeak (Figs. 8c). Although the heaviest rainfall events exhibit the highest mean rainfall intensity, Imean (Fig. 8d), the difference in the peak rain rate, Ipeak (Fig. 8e), between the events with upper and lower ranks is more pronounced than for Imean. Precipitation during the hour of peak rain rate, Ppeak, constitutes a large part (> 40%) of the total rainfall, Ptotal, for most (90%) of the events. The ratio, Ppeak/Ptotal (Fig. 8f), decreases with the ranking of the events, consistent with the increase in the event duration, Dtotal (Fig. 8a).

In Future-Warming, the durations of the heavy rainfall events, D_{total} , do not differ significantly from Current-Climate (Fig. 8a). The storm propagating speed, V_{peak} , and storm area, A_{peak} , at the time of the peak rain rate are both significantly larger in Future-Warming than in Current-Climate (Figs. 8b-c). They produce competing effects on the duration of the events. The mean (peak) rainfall intensity, I_{mean} (I_{peak}), is higher by \sim 8 (17) mm hr⁻¹, and primarily contributes to the higher rainfall totals of the events in Future-Warming than in Current-Climate (Figs. 8d-e). P_{peak}/P_{total} is similar between the two ensemble experiments (Fig. 8f).

Figure 9 shows the ensemble mean differences in low and mid-level moisture, horizontal winds, and vertical wind shear between Future-Warming and Current-Climate. At 925 hPa (Fig. 9a), there is a significant increase in specific humidity in Future-Warming - values ~5 g kg⁻¹ higher than Current Climate over the Sahel with the largest anomalies near the Marrah Mountains (10°N - 18°N, 15°E - 34°E). This increase in low-level moisture occurs with anomalous southwesterlies between 14°N – 19°N east of 10°E, indicating increased poleward transport of low-level moist tropical air into the central and eastern Sahel. This wind and moisture advection pattern is associated with the strong surface warming over the central and eastern Sahara (Cook and Vizy 2015; Vizy and Cook 2017) and higher rain rates over the Sahel (Vizy et al. 2013) in the future.

At 600 hPa (Fig. 9b), specific humidity increases by >2 g kg⁻¹ over the southern Sahel and the northern Sahel east of 8°E in Future-Warming. The AEJ is stronger by 1-6 m s⁻¹, with the largest increases in the eastern Sahel. The circulation anomalies contribute to a 1-10 m s⁻¹ increase in the 600 hPa - 925 hPa zonal vertical wind shear over the analysis region in the future (Fig. 9c).

In summary, the frequency of heavy rainfall events during August increases over the analysis region in Future-Warming compared to Current-Climate. The heaviest rainfall events in Future-Warming have ~8 (17) mm hr⁻¹ higher mean (peak) rainfall intensity, and ~59% and ~31%

larger storm rain-shield area and propagating speed at the time of the peak rain rate, but the durations of the events do not differ significantly between the two experiments. Both atmospheric moisture and vertical wind shear increase over the Sahel in the Future-Climate simulation. The physical processes responsible are examined in the following sub-section.

c. Shear versus Thermodynamic Effects on Heavy Rainfall Events

To isolate and identify the pre-storm environment, Figure 10 shows the time series of vertical wind shear and low- to mid-level zonal wind, moisture, and temperature for the storm and dry-day composites from Current-Climate and Future-Warming. The dry-day composite is used as a control comparison to storm-day conditions to exclude confounding effects such as diurnal variations. The dry-day composite is formed by averaging dry-day conditions at the location of each event, when 12Z-12Z 24-hr precipitation totals over a 45x45-km² area centered at the location of the event is < 10 mm day¹. Dry-day conditions for each event are derived using the ensemble member that contains the event. The 600-hPa to 925-hPa vertical wind shear speed (Fig. 10a) decreases as the storm passes, reaching a minimum around the time of the peak rain rate. The decrease in the shear speed occurs with a sharp change in the shear direction.

Figure 10b illustrates how storm processes affect the environmental vertical wind shear at low- and mid-levels. At 925 hPa, the storm's cold pool affects the direction of the westerly monsoonal flow as the storm passes. At the 600 hPa, the storms' convective updrafts weaken the AEJ easterlies. In addition, inflow into the storm may enhance the shear strength as the storm approaches, but this effect is relatively weak and varies among the storms (not shown).

Low- to mid-level moisture and precipitable water increase as the storm approaches (Fig. 10c). Preconditioning of the precipitable water starts 12 hours or more prior to ~59% of the events

(not shown). After the peak rain rate, the 800-hPa moisture decreases below that of the dry days in association with downdrafts. The passage of the storm's cold pool is also linked to a decrease in the lower-tropospheric temperature, and the mid-tropospheric temperature increases with the latent heat release of the storm (Fig. 10d). These characteristics of the storm-environment interaction are similar in the Future-Warming storms (Figs. 10e-h) despite the higher vertical wind shear, moisture, and temperature.

In summary, environmental conditions are largely unperturbed by the storm dynamics 3 hours before the peak rain rate of heavy events. This is consistent with previous studies (Taylor et al. 2017; Fitzpatrick et al. 2020; Vizy and Cook 2022). To account for variability among the events, we compute pre-storm environmental conditions when rainfall intensity over the 45x45-km² area centered at the location of the events first falls below 10 mm day¹ prior to the peak rain rate of the events. The trackback time before the peak rain rate is within 1-3 hours for 84% (83%) of the events from Current-Climate (Future-Warming), consistent with the results shown in Fig. 10.

Figures 11a-e show vertical profiles of the environmental vertical wind shear and thermodynamic conditions for the storm and dry-day composites from Current-Climate. The composite of ensemble mean conditions at the location of each event has similar vertical profiles to the dry-day composite (not shown). Low-level westerlies and mid-tropospheric easterlies (northerlies) in the storm composite are 2.4 m s⁻¹ stronger and 2.5 (0.95) m s⁻¹ weaker (stronger) than the dry-day composite, respectively (Figs. 11a-b). This is accomplished by a strong monsoonal flow and a weak AEJ before most (~74-79%) of the heavy rainfall events (not shown). The 800 hPa – 600 hPa MSE is also ~33% higher in the storm composite compared to the dry-day composite (Fig. 11c), indicating greater environmental instability prior to the heavy rainfall events. Higher instability is also indicated by greater (smaller) CAPE (CIN) in the storm composite, which

is 468 (17) J kg⁻¹ higher (lower) than the dry-day composite at 850 hPa (Figs. 11d-e). Although there is a wide range of variability between individual events for both the storm and dry-day composites, significant differences between the two composites are representative of most (60-92%) of the event-specific differences (not shown).

Differences between the storm and dry-day composites in Future-Warming (Figs. 11f-j) are generally similar to those in Current-Climate. In the storm composite of Future-Warming, the magnitudes of the 600-hPa easterlies (northerlies) and the 925-hPa westerlies are 1.8 (1.7) and 0.96 m s⁻¹ larger than Current-Climate (Figs. 11f-g). These differences occur through the enhanced AEJ and monsoonal flow in Future-Warming (Fig. 9), and contribute to a 3.2 m s⁻¹ increase in the 600 hPa – 925 hPa vertical wind shear prior to the heavy rainfall events. MSE is higher throughout the troposphere in Future-Warming compared to Current-Climate, with 800 hPa – 600 hPa MSE ~22% larger in the future (Fig. 11h). This is consistent with the ~500 J kg⁻¹ increase in 850-hPa CAPE in Future-Warming (Fig. 11i). Enhanced CIN in the future (Fig. 11j) suppresses weak convection, favoring the buildup of environmental instability for intense rainfall.

Table 5a shows correlations between the shear indices (Table 2) and the rainfall/storm metrics (Table 1) for the selected heavy rainfall events from Current-Climate. Correlations between the vertical wind shear strength, du, dv, and $S_{magnitude}$, and the storm's convective or rainfall intensity, ω_{peak} and I_{peak} , are insignificant, although significant but weak anti-correlations are shown between the shear strength and the level of maximum updraft velocity, H_{ω} . The following discussion will not specifically introduce such weak, significant correlations, but will be more focused on relatively high, significant correlations. Compared to correlations with storm intensity, correlations of the shear strength with the storm's rain-shield area and propagating speed have higher magnitudes and statistical significance. The area of the storm's rain shield, $A_{convective}$

or $A_{stratiform}$, increases with the shear strength, and so does the storm propagating speed at the time of the peak rain rate, V_{peak} . Thus, the low- to mid-level vertical environmental wind shear does not impact storm intensity for the evaluated events in our simulations but has roles in enhancing the storm's organization and propagation (Corfidi 2003; Mulholland et al. 2021). The results of Future-Warming (Table 5b) are generally similar to those of Current-Climate.

507

508

509

510

511

512

513

514

515

516

517

518

519

520

521

522

523

524

525

526

527

528

529

Table 6 shows correlations between the thermodynamic indices (Table 2) and the rainfall/storm metrics for the selected heavy rainfall events from Current-Climate. Lower tropospheric specific humidity, q₈₀₀, is correlated with the maximum updraft velocity and the peak rain rate of the event, ω_{peak} and I_{peak} . In contrast, significant anti-correlations exist between middle tropospheric specific humidity, q_{600} , and storm intensity, ω_{peak} and I_{peak} . The opposite signs of these correlations are consistent with the relatively strong link between the moisture vertical gradient, q_{gradient}, and storm intensity. In comparison, precipitable water, PW, has weak or insignificant correlations with ω_{peak} and I_{peak} . Similar to the moisture indices, low- (mid-) level temperature, T₈₀₀ (T₆₀₀), and the temperature vertical gradient, T_{gradient}, are (inversely) related to the storm's convective intensity, ω_{peak} . However, this relationship does not translate into significant correlations between the temperature indices and the peak rain rate, Ipeak, for the storm population selected from Current-Climate. The correlations of the moisture and temperature indices imply a close connection between atmospheric instability and the storm's convective or rainfall intensity. This is directly shown by the significant correlations of MSE_{gradient}, CAPE₈₅₀, and CIN₈₅₀ with ω_{peak} and I_{peak}. Overall, correlations of thermodynamic conditions have higher magnitudes than those of the vertical wind shear with storm intensity (Table 5).

Apart from storm intensity, thermodynamic conditions are related to the storm's rain-shield area and propagating speed. The storm's rain-shield area at the time of the peak rain rate, $A_{convective}$

and A_{stratiform}, increase with low-tropospheric temperature (and moisture) as well as atmospheric instability, T₈₀₀, q₈₀₀, q_{gradient}, T_{gradient}, MSE_{gradient}, CAPE₈₅₀, and/or CIN₈₅₀. In addition, enhanced atmospheric instability and low-tropospheric CIN are related to a faster storm propagating speed, V_{peak}. Correlations derived from Future-Warming (Table 6b) show similar signs, magnitude, and/or significance levels to those from Current-Climate in general.

Tables 7-8 also show correlations between environmental conditions and rainfall/storm metrics, but the shear and thermodynamic indices are derived 3 hours prior to the peak rain rate of each event to test the dependence of the results on the definition of pre-storm environmental conditions. Results are generally similar to those in Tables 5-6, although weak but significant correlations occur between the shear strength and the peak rain rate in Table 7. Thus, caution is appropriate to interpret the correlations. Our discussion is mainly based on Tables 5-6, since the shear indices in Table 5 are more sophisticated to exclude the effects of storm dynamics by considering variability among the storms. The correlations in Tables 5-8 generally do not show high magnitudes, implying impacts of storm dynamics and life cycle on local rainfall events.

The selected heavy rainfall events from Current-Climate and Future-Warming are separated into groups of similar vertical wind shear to assess the thermodynamic contribution to rainfall intensification over the West African Sahel. Despite the increase in the average shear strength between Current-Climate and Future-Warming (Figs. 10-11), the ranges of the shear strength overlap to a large extent between the two experiments (Figure 12a). Thus, the events are divided into four groups using a 5 m s⁻¹ (~1 standard deviation in either experiment) interval of 600 hPa – 925 hPa zonal wind difference, du (Table 2), to ensure a sufficient number of events and similar vertical wind shear conditions within each group. The mean zonal vertical wind shear, du,

is -12.25 (-15.05) m s^{-1} in Current-Climate (Future-Warming), located in the 3^{rd} group. Shear strength in the $1^{st}/4^{th}$ group is about 1.5/1 standard deviation higher/lower than the mean values.

For each group of events, the zonal vertical wind shear, du, or the shear strength, $S_{magnitude}$, is similar between the Future-Warming and Current-Climate experiments. Table 9a shows that the maximum absolute (relative) difference between the two experiments is -0.42 m s⁻¹ (5.21%) for du and 1.09 m s⁻¹ (6.04%) for $S_{magnitude}$, respectively. Keeping du relatively constant also limits the variations in the meridional vertical wind shear, dv, except the 2^{nd} group.

Difference in the thermodynamic conditions between Future-Warming and Current-Climate are shown in Fig. 12b and Table 9b for the four groups of events. The 800-hPa specific humidity, q_{800} , increases by 22.87-30.17% in the future. This approximates the 7% K⁻¹ CC scaling, as the 800-hPa temperature, T_{800} , increases by 3.65-4.07 K. The scaling of precipitable water is super-CC, since the mid-level moisture, q_{600} , increases at rates of 9.25-12.34% K⁻¹.

The scaling of the peak rain rate, I_{peak} , does not exactly follow the relative increase in the low-level moisture or precipitable water between Future-Warming and Current-Climate (Fig. 12b). The relative increase of I_{peak} ranges from 5.88% to 37.76%, far below (above) the 7% K^{-1} CC scaling in the 1^{st} (4^{th}) group of events with strong (weak) vertical wind shear. The scaling of I_{peak} has similar magnitudes to the relative difference in the MSE vertical gradient, MSE_{gradient}, across the storm groups. Thus, variations in atmospheric instability due to greenhouse gas increases constrain (enhance) the rainfall intensification over the Sahel under strong (weak) shear conditions.

To explore why the relative difference in $MSE_{gradient}$ varies with the shear strength, Table 10 shows correlations between the shear and thermodynamic indices for the selected heavy rainfall events. Figure 12c illustrates relationships discussed below. The Current-Climate $MSE_{gradient}$, as the denominator of the relative difference in $MSE_{gradient}$, increases with the vertical wind shear.

This is sourced from the relationship between the shear strength and the latent and thermal components of MSE. Specifically, 600-hPa moisture and precipitable water, q₆₀₀ and PW, decrease with the shear strength in Current-Climate. The 800-hPa (600-hPa) temperature, T₈₀₀ (T₆₀₀), is (anti-) correlated with the shear strength in both Current-Climate and Future-Warming. A potential underlying mechanism is that northeasterlies associated with the AEJ transport more dry, warmer air at 800 hPa and dry, cooler air at 600 hPa from the Sahara into the Sahel with strong vertical wind shear, and vice versa. With greenhouse gas increases, specific humidity increases less over the Sahara than over the Sahel (Fig. 9). This may contribute to the small increase in the 800-hPa moisture, q₈₀₀, and further the small difference in the MSE vertical gradient, MSE_{gradient}, under strong shear, while the opposite is true under weak shear.

Since there is little overlap in the thermodynamic conditions between the current and future climate, a similar assessment cannot be conducted to delineate the dynamic contribution to the intensified rainfall over the West African Sahel with increasing greenhouse gas levels. However, the analysis of Fig. 12 and Tables 9-10 still implies a primary contribution from the thermodynamic processes to storm intensification over the Sahel. The $2^{nd} - 4^{th}$ groups (Fig. 12) contain 84 (80) % of the selected heavy rainfall events from Current-Climate (Future-Warming), and the average peak rain rates of these groups increase by 21-38% (15-26 mm) in the future with the primary contribution from thermodynamic processes. These increased magnitudes are similar to the scaling of I_{peak} for all the events under enhanced vertical wind shear (24%, 17 mm) in the simulations.

In summary, thermodynamic conditions are more closely related to greenhouse gas-forced storm intensification and increased frequency over the West African Sahel than changes in the vertical wind shear. Although both factors are related to the storms' rain-shield areas, propagating

speeds, and the duration of the rainfall events, the simulated heavier rainfall across the Sahel is primarily linked to higher rainfall intensity rather than a longer duration of events.

5 Conclusions

The West African Sahel is known for the frequent occurrence of intense storms and catastrophic floods that lead to severe socioeconomic loss. The low-level southwesterly monsoonal flow and the mid-tropospheric AEJ generate strong vertical wind shear over the Sahel during boreal summer, forming a unique dynamic environment for storm evolution. The frequency of intense storms over this region has been observed to be increasing in recent decades (Taylor et al. 2017; Chagnaud et al. 2022) and the trend is projected to continue throughout the 21st century with global warming. The purpose of our study is to understand the relative importance of the dynamic and thermodynamic processes for this greenhouse gas-induced rainfall intensification.

Our study uses ensemble simulations with the WRF regional atmospheric model with triple-nested (27/9/3-km) domains (Fig. 2) to represent the current and future August climatology over the West and Central Africa. Cumulus parameterization is turned off in the 3-km (CP) domain, which covers much of Sahel and is the focus of the analysis. The "Current-Climate" experiment consists of 16 ensemble members, with initial and boundary conditions from the ERA5 reanalysis and OSTIA SST observations. Five "Future-Warming" simulations represent late-21st-century conditions under the IPCC's SSP585 scenario, which hypothesizes fossil-fueled development. Initial and lateral boundary conditions for the future simulations are generated by adding multimodel mean anomalies derived from CMIP6 simulations to the ERA5 values. The large outer domain eliminates influence from the lateral boundary anomalies in the CP domain, and the primary climate change forcing is from increases in greenhouse gases.

Hourly output from the CP domain is used to analyze storm evolution and relevant environmental conditions. We identify heavy rainfall events that produce the highest 24-hr rainfall totals following the method of Vizy and Cook (2022). Rainfall/storm indices (Table 1) are developed to quantify the characteristics of the events, such as duration, peak rain rate, etc. Metrics (Table 2) are also derived for pre-storm environmental shear and thermodynamic conditions.

The Current-Climate simulation generally reproduces observed August rainfall, moisture, and circulation patterns, although it has relatively dry conditions across the northern Sahel. The simulated frequency curve of 24-hr rainfall totals over the analysis region is similar to the IMERG observations. The 99.9th percentile rainfall totals are 77 mm in Current-Climate and 89 mm in IMERG. Current-Climate realistically represents the spatial and frequency distributions of heavy rainfall events over the analysis region. Most of the heaviest rainfall events are located south of 15°N over a few cluster regions, consistent with Vizy and Cook (2022). In addition, the simulations capture low- to mid-tropospheric features well, such as the meridional moisture gradient, the AEJ, and the vertical wind shear, compared to ERA5.

In Future-Warming, the ensemble mean August precipitation increases by ~2 mm day⁻¹ over the Sahel, with the maximum anomalies centered in the eastern part of the domain. Rainfall decreases over the Guinean Highlands, the Cameroon Highlands, and tropical Central Africa. The spatial distribution of heavy rainfall events over the analysis region is similar between Current-Climate and Future-Warming. The frequency of events with 24-hr rainfall totals above 77 mm increases by ~20 events per month in the future, exceeding the range of ensemble member variability of Current-Climate. Analysis the top 30 events selected from each ensemble simulation of Current-Climate and Future-Warming indicate that the increase in rainfall totals is primarily related to an increase in rainfall intensity rather than the duration of events.

Rainfall intensification occurs primarily through thermodynamics processes, and not through dynamical processes related to changes in the vertical wind shear. Environmental conditions prior to heavy rainfall events have significant differences from dry-day (and climatological) conditions, including relatively strong low-level westerlies, weak mid-level easterlies, and high atmospheric instability. In the storm composites, the environmental vertical wind shear prior to the events is 3.2 m s⁻¹ higher in Future-Warming than in Current-Climate, with the 800 hPa – 600 hPa MSE vertical gradient (850-hPa CAPE) enhanced by ~22% (~500 J kg⁻¹). Despite these differences, wind shear strength is not correlated with peak rain rates. In contrast, thermodynamic features – especially measures of atmospheric instability related to lower/middle tropospheric moisture and temperature - have high, significant correlations with storm intensity. This indicates the dominant role of the thermodynamic process in intensifying the rainfall over the Sahel. This finding is consistent with several previous studies (Bickle et al. 2020; Fitzpatrick et al. 2020) and inconsistent with others (Taylor et al. 2017; Baidu et al. 2022).

The environmental vertical wind shear along with thermodynamic conditions is linked to a larger rain-shield area and propagation speed of the storms, and this can affect the duration and total precipitation of events. The duration of events is not significantly different between the current and future simulations with enhanced vertical wind shear over the Sahel, but this mechanism may be influential for other regions of the world. In addition, the vertical wind shear is connected with thermodynamic conditions. Strong wind shear is related to high environmental instability, transporting more dry, warm (cool) lower (middle) tropospheric air from the Sahara into the Sahel, while the opposite occurs with weak wind shear. Increased greenhouse gas levels induce a small difference in atmospheric instability for Sahelian storms under strong vertical wind

shear, which constrains rainfall intensification of such storms. By contrast, atmospheric instability rises under weak wind shear, enhancing intensification of heavy precipitation over the Sahel.

Our analysis does not corroborate the close relationship between shear strength and storm intensity as is found in idealized experiments (e.g., Weisman and Rotunno 2004), and several factors may be relevant. First, the environmental vertical wind shear or its interactions with the storm's cold pool may not be sufficiently different between the current and future climate to generate significant impacts on rain rates. Moreover, the deepest convection does not necessarily signify the most intense rainfall (Hamada et al. 2015; Hamada and Takayabu 2018), and MCSs often include multiple convective cores mixed with stratiform areas. Thus, the proposed theory that an "optimal" shear strength favors deeper convection may not translate into a connection between environmental shear strength and the storm's surface rainfall rates. Furthermore, complexities are involved in measuring environmental vertical wind shear in realistic simulations, and the shear direction and strength may vary across a storm front. The depth/height of the vertical wind shear and the alignment between the shear and the storms' propagating directions also vary. Finally, we have not excluded the possibility that vertical wind shear has a more obvious control over rainfall intensity for storms with certain characteristics or over specific regions. This can be studied with future improvement in storm observations and model simulations.

These results have general implications for understanding the climatology or variability of storms in other regions. Additional work is required to further understand the relevant physical processes that underlie the correlations and to evaluate the sensitivity of the results to storm life cycle, diurnal cycle timing, locations, short-term SST variability, etc.

686

687

665

666

667

668

669

670

671

672

673

674

675

676

677

678

679

680

681

682

683

684

685

Acknowledgements

688	Support from NSF Award #1929074 is gratefully acknowledged. The HPC and database
689	resources needed for the analysis were supplied by the Texas Advanced Computing Center (TACC)
690	at The University of Texas at Austin. URL: http://www.tacc.utexas.edu .
691	
692	References
693	Alfaro DA (2017) Low-tropospheric shear in the structure of squall lines: Impacts on latent
694	heating under layer-lifting ascent. J Atmos Sci 74:229–248. https://doi.org/10.1175/JAS-D-
695	16-0168.1
696	Alfaro DA, Khairoutdinov M (2015) Thermodynamic constraints on the morphology of
697	simulated midlatitude squall lines. J Atmos Sci 72:3116–3137. https://doi.org/10.1175/JAS-
698	D-14-0295.1
699	Argent R, Sun X, Semazzi F, et al (2015) The Development of a Customization Framework for
700	the WRF Model over the Lake Victoria Basin, Eastern Africa on Seasonal Timescales.
701	Advances in Meteorology 2015:653473. https://doi.org/10.1155/2015/653473
702	Baidu M, Schwendike J, Marsham JH, Bain C (2022) Effects of vertical wind shear on intensities
703	of mesoscale convective systems over West and Central Africa. Atmospheric Science
704	Letters 23:e1094. https://doi.org/https://doi.org/10.1002/asl.1094
705	Bercos-Hickey E, Patricola CM (2021) Anthropogenic influences on the African easterly jet-
706	African easterly wave system. Clim Dyn 57:2779–2792. https://doi.org/10.1007/s00382-
707	021-05838-1
708	Berthou S, Kendon EJ, Rowell DP, et al (2019) Larger Future Intensification of Rainfall in the
709	West African Sahel in a Convection-Permitting Model. Geophys Res Lett 46:13299–13307.
710	https://doi.org/10.1029/2019GL083544

711	Bichet A, Diedhiou A (2018) West African Sahel has become wetter during the last 30 years, but
712	dry spells are shorter and more frequent. Clim Res 75:155–162.
713	https://doi.org/10.3354/cr01515
714	Bickle ME, Marsham JH, Ross AN, et al (2020) Understanding mechanisms for trends in
715	Sahelian squall lines: Roles of thermodynamics and shear. Quarterly Journal of the Royal
716	Meteorological Society 983-1006. https://doi.org/10.1002/qj.3955
717	Chagnaud G, Panthou G, Vischel T, Lebel T (2022) A synthetic view of rainfall intensification in
718	the West African Sahel. Environmental Research Letters 17:. https://doi.org/10.1088/1748-
719	9326/ac4a9c
720	Chen D, Rojas M, Samset BH, et al (2021) Framing, Context, and Methods. In: Masson-
721	Delmotte V, Zhai P, Pirani A, et al. (eds) Climate Change 2021: The Physical Science
722	Basis. Contribution of Working Group I to the Sixth Assessment Report of the
723	Intergovernmental Panel on Climate Change. Cambridge University Press, Cambridge,
724	United Kingdom and New York, NY, USA, pp 147-286
725	Chen F, Dudhia J (2001) Coupling and advanced land surface-hydrology model with the Penn
726	State-NCAR MM5 modeling system. Part I: Model implementation and sensitivity. Mon
727	Weather Rev 129:569–585. https://doi.org/10.1175/1520-
728	0493(2001)129<0569:CAALSH>2.0.CO;2
729	Chen Q, Fan J, Hagos S, et al (2015) Roles of wind shear at different vertical levels: Cloud
730	system organization and properties. Journal of Geophysical Research: Atmospheres
731	120:6551–6574. https://doi.org/https://doi.org/10.1002/2015JD023253

732	Coniglio MC, Corfidi SF, Kain JS (2012) Views on applying RKW theory: An illustration using
733	the 8 may 2009 derecho-producing convective system. Mon Weather Rev 140:1023–1043.
734	https://doi.org/10.1175/MWR-D-11-00026.1
735	Cook KH (1999) Generation of the African easterly jet and its role in determining West African
736	precipitation. J Clim 12:1165-1184. https://doi.org/10.1175/1520-
737	0442(1999)012<1165:GOTAEJ>2.0.CO;2
738	Cook KH, Vizy EK (2019) Contemporary Climate Change of the African Monsoon Systems.
739	Curr Clim Change Rep 5:145–159. https://doi.org/10.1007/s40641-019-00130-1
740	Cook KH, Vizy EK (2015) Detection and Analysis of an Amplified Warming of the Sahara
741	Desert. J Clim 28:6560-6580. https://doi.org/10.1175/JCLI-D-14-00230.1
742	Cook KH, Vizy EK (2012) Impact of climate change on mid-twenty-first century growing
743	seasons in Africa. Clim Dyn 39:2937–2955. https://doi.org/10.1007/s00382-012-1324-1
744	Corfidi SF (2003) Cold Pools and MCS Propagation: Forecasting the Motion of Downwind-
745	Developing MCSs. Weather Forecast 18:997–1017.
746	https://doi.org/https://doi.org/10.1175/1520-0434(2003)018<0997:CPAMPF>2.0.CO;2
747	Crétat J, Vizy EK, Cook KH (2015) The relationship between African easterly waves and daily
748	rainfall over West Africa: observations and regional climate simulations. Clim Dyn 44:385-
749	404. https://doi.org/10.1007/s00382-014-2120-x
750	di Baldassarre G, Montanari A, Lins H, et al (2010) Flood fatalities in Africa: From diagnosis to
751	mitigation. Geophys Res Lett 37:. https://doi.org/https://doi.org/10.1029/2010GL045467
752	Dezfuli AK, Ichoku CM, Mohr KI, Huffman GJ (2017) Precipitation Characteristics in West and
753	East Africa from Satellite and in Situ Observations. J Hydrometeorol 18:1799–1805.
754	https://doi.org/https://doi.org/10.1175/JHM-D-17-0068.1

755	Dong B, Sutton R (2015) Dominant role of greenhouse-gas forcing in the recovery of Sahel
756	rainfall. Nat Clim Chang 5:757-760. https://doi.org/10.1038/nclimate2664
757	Donlon CJ, Martin M, Stark J, et al (2012) The Operational Sea Surface Temperature and Sea
758	Ice Analysis (OSTIA) system. Remote Sens Environ 116:140–158.
759	https://doi.org/https://doi.org/10.1016/j.rse.2010.10.017
760	Dosio A, Jones RG, Jack C, et al (2019) What can we know about future precipitation in Africa?
761	Robustness, significance and added value of projections from a large ensemble of regional
762	climate models. Clim Dyn 53:5833-5858. https://doi.org/10.1007/s00382-019-04900-3
763	Dosio A, Turner AG, Tamoffo AT, et al (2020) A tale of two futures: Contrasting scenarios of
764	future precipitation for West Africa from an ensemble of regional climate models.
765	Environmental Research Letters 15:. https://doi.org/10.1088/1748-9326/ab7fde
766	Doswell CA, Brooks HE, Maddox RA (1996) Flash Flood Forecasting: An Ingredients-Based
767	Methodology. Weather Forecast 11:560–581. https://doi.org/10.1175/1520-
768	0434(1996)011<0560:FFFAIB>2.0.CO;2
769	Dudhia J (1989) Numerical Study of Convection Observed during the Winter Monsoon
770	Experiment Using a Mesoscale Two-Dimensional Model. Journal of Atmospheric Sciences
771	46:3077–3107. https://doi.org/10.1175/1520-0469(1989)046<3077:NSOCOD>2.0.CO;2
772	EC-Earth (2019) EC-Earth-Consortium EC-Earth3 model output prepared for CMIP6 CMIP
773	historical. Earth System Grid Federation. https://doi.org/10.22033/ESGF/CMIP6.4700
774	Eldridge RH (1957) A synoptic study of west african disturbance lines. Quarterly Journal of the
775	Royal Meteorological Society 83:303–314.
776	https://doi.org/https://doi.org/10.1002/qj.49708335704

777	Eyring V, Bony S, Meehl GA, et al (2016) Overview of the Coupled Model Intercomparison
778	Project Phase 6 (CMIP6) experimental design and organization. Geosci Model Dev 9:1937-
779	1958. https://doi.org/10.5194/gmd-9-1937-2016
780	Finney DL, Marsham JH, Jackson LS, et al (2019) Implications of improved representation of
781	convection for the East Africa water budget using a convection-permitting model. J Clim
782	32:2109–2129. https://doi.org/10.1175/JCLI-D-18-0387.1
783	Fischer EM, Knutti R (2016) Observed heavy precipitation increase confirms theory and early
784	models. Nat Clim Chang 6:986–991. https://doi.org/10.1038/nclimate3110
785	Fitzpatrick RGJ, Parker DJ, Marsham JH, et al (2020) What drives the intensification of
786	mesoscale convective systems over the West African Sahel under climate change? J Clim
787	33:3151–3172. https://doi.org/10.1175/JCLI-D-19-0380.1
788	Fox-Kemper B, Hewitt H, Xiao C, et al (2021) Chapter 9: Ocean, Cryosphere and Sea Level
789	Change. In: Masson-Delmotte V, Zhai P, Pirani A, et al. (eds) Climate Change 2021: The
790	Physical Science Basis. Contribution of Working Group I to the Sixth Assessment Report of
791	the Intergovernmental Panel on Climate Change. Cambridge University Press, pp 1–257
792	Guo H, John JG, Blanton C, et al (2018) NOAA-GFDL GFDL-CM4 model output. Earth System
793	Grid Federation. https://doi.org/10.22033/ESGF/CMIP6.1402
794	Haerter JO, Schlemmer L (2018) Intensified Cold Pool Dynamics Under Stronger Surface
795	Heating. Geophys Res Lett 45:6299–6310.
796	https://doi.org/https://doi.org/10.1029/2017GL076874
797	Hagos SM, Cook KH (2007) Dynamics of the West African Monsoon Jump. J Clim 20:5264-
798	5284. https://doi.org/10.1175/2007JCLI1533.1

799	Hamada A, Takayabu YN (2018) Large-scale environmental conditions related to midsummer
800	extreme rainfall events around Japan in the TRMM region. J Clim 31:6933-6945.
801	https://doi.org/10.1175/JCLI-D-17-0632.1
802	Hamada A, Takayabu YN, Liu C, Zipser EJ (2015) Weak linkage between the heaviest rainfall
803	and tallest storms. Nat Commun 6:1-6. https://doi.org/10.1038/ncomms7213
804	Hersbach H, Bell B, Berrisford P, et al (2020) The ERA5 global reanalysis. Quarterly Journal of
805	the Royal Meteorological Society 146:1999–2049.
806	https://doi.org/https://doi.org/10.1002/qj.3803
807	Hong SY, Noh Y, Dudhia J (2006) A new vertical diffusion package with an explicit treatment
808	of entrainment processes. Mon Weather Rev 134:2318–2341.
809	https://doi.org/10.1175/MWR3199.1
810	Huffman G, Stocker E, Bolvin D, et al (2019) GPM IMERG Final Precipitation L3 Half Hourly
811	0.1 degree x 0.1 degree V06. Greenbelt, MD
812	Hutchinson TA (2009) An Adaptive Time-Step for Increased Model Efficiency. Extended
813	Abstracts, Eighth WRF Users' Workshop 4
814	Iyakaremye V, Zeng G, Siebert A, Yang X (2021) Contribution of external forcings to the
815	observed trend in surface temperature over Africa during 1901-2014 and its future
816	projection from CMIP6 simulations. Atmos Res 254:105512.
817	https://doi.org/10.1016/j.atmosres.2021.105512
818	Jeworrek J, West G, Stull R (2019) Evaluation of cumulus and microphysics parameterizations
819	in WRF across the convective gray zone. Weather Forecast 34:1097–1115.
820	https://doi.org/10.1175/WAF-D-18-0178.1

821	Jiménez PA, Dudhia J, González-Rouco JF, et al (2012) A Revised Scheme for the WRF Surface
822	Layer Formulation. Mon Weather Rev 140:898–918. https://doi.org/10.1175/MWR-D-11-
823	00056.1
824	Kain JS (2004) The Kain-Fritsch Convective Parameterization: An Update. Journal of Applied
825	Meteorology 43:170–181. https://doi.org/10.1175/1520-
826	0450(2004)043<0170:TKCPAU>2.0.CO;2
827	Kebe I, Diallo I, Sylla MB, et al (2020) Late 21st century projected changes in the relationship
828	between precipitation, African Easterly Jet, and African Easterly Waves. Atmosphere
829	(Basel) 11:. https://doi.org/10.3390/atmos11040353
830	Kendon EJ, Stratton RA, Tucker S, et al (2019) Enhanced future changes in wet and dry
831	extremes over Africa at convection-permitting scale. Nat Commun 10:.
832	https://doi.org/10.1038/s41467-019-09776-9
833	Klutse NAB, Quagraine KA, Nkrumah F, et al (2021) The Climatic Analysis of Summer
834	Monsoon Extreme Precipitation Events over West Africa in CMIP6 Simulations. Earth
835	Systems and Environment 5:25-41. https://doi.org/10.1007/s41748-021-00203-y
836	Laing AG, Fritsch JM, Negri AJ (1999) Contribution of Mesoscale Convective Complexes to
837	Rainfall in Sahelian Africa: Estimates from Geostationary Infrared and Passive Microwave
838	Data. Journal of Applied Meteorology 38:957-964. https://doi.org/10.1175/1520-
839	0450(1999)038<0957:COMCCT>2.0.CO;2
840	Laing AG, Trier SB, Davis CA (2012) Numerical simulation of episodes of organized
841	convection in tropical Northern Africa. Mon Weather Rev 140:2874–2886.
842	https://doi.org/10.1175/MWR-D-11-00330.1

843	Laurent H, D'Amato N, Lebel T (1998) How important is the contribution of the mesoscale
844	convective complexes to the Sahelian rainfall? Physics and Chemistry of the Earth 23:629-
845	633. https://doi.org/https://doi.org/10.1016/S0079-1946(98)00099-8
846	Lavaysse C (2015) Saharan desert warming. Nat Clim Chang 5:807–808.
847	https://doi.org/10.1038/nclimate2773
848	Lavaysse C, Flamant C, Janicot S (2010) Regional-scale convection patterns during strong and
849	weak phases of the Saharan heat low. Atmospheric Science Letters 11:255-264.
850	https://doi.org/https://doi.org/10.1002/asl.284
851	Lenderink G, Barbero R, Loriaux JM, Fowler HJ (2017) Super-Clausius-Clapeyron Scaling of
852	Extreme Hourly Convective Precipitation and Its Relation to Large-Scale Atmospheric
853	Conditions. J Clim 30:6037–6052. https://doi.org/https://doi.org/10.1175/JCLI-D-16-0808.1
854	Lenderink G, de Vries H, Fowler HJ, et al (2021) Scaling and responses of extreme hourly
855	precipitation in three climate experiments with a convection-permitting model.
856	Philosophical Transactions of the Royal Society A: Mathematical, Physical and Engineering
857	Sciences 379:20190544. https://doi.org/10.1098/rsta.2019.0544
858	Liu C, Ikeda K, Rasmussen R, et al (2017) Continental-scale convection-permitting modeling of
859	the current and future climate of North America. Clim Dyn 49:71-95.
860	https://doi.org/10.1007/s00382-016-3327-9
861	Liu W, Cook K, Vizy E (2020) Influence of Indian Ocean SST regionality on the East African
862	short rains. Clim Dyn. https://doi.org/10.1007/s00382-020-05265-8
863	Liu W, Cook KH, Vizy EK (2019) The role of mesoscale convective systems in the diurnal cycle
864	of rainfall and its seasonality over sub-Saharan Northern Africa. Clim Dyn 52:729-745.
865	https://doi.org/10.1007/s00382-018-4162-y

866	Lochbihler K, Lenderink G, Siebesma AP (2021) Cold Pool Dynamics Shape the Response of
867	Extreme Rainfall Events to Climate Change. J Adv Model Earth Syst 13:e2020MS002306.
868	https://doi.org/https://doi.org/10.1029/2020MS002306
869	Loriaux JM, Lenderink G, De Roode SR, Siebesma AP (2013) Understanding Convective
870	Extreme Precipitation Scaling Using Observations and an Entraining Plume Model. J Atmos
871	Sci 70:3641–3655. https://doi.org/https://doi.org/10.1175/JAS-D-12-0317.1
872	Maidment RI, Allan RP, Black E (2015) Recent observed and simulated changes in precipitation
873	over Africa. Geophys Res Lett 42:8155–8164.
874	https://doi.org/https://doi.org/10.1002/2015GL065765
875	Makinde AI, Abiodun BJ, James R, et al (2022) How Well Do CMIP6 Models Simulate the
876	Influence of the West African Westerly Jet on Sahel Precipitation? ResearchSquare 1–20.
877	https://doi.org/10.21203/rs.3.rs-1274137
878	Mathon V, Laurent H, Lebel T (2002) Mesoscale convective system rainfall in the Sahel. Journal
879	of Applied Meteorology 41:1081–1092. https://doi.org/10.1175/1520-
880	0450(2002)041<1081:MCSRIT>2.0.CO;2
881	Mlawer EJ, Taubman SJ, Brown PD, et al (1997) Radiative transfer for inhomogeneous
882	atmospheres: RRTM, a validated correlated-k model for the longwave. Journal of
883	Geophysical Research: Atmospheres 102:16663–16682.
884	https://doi.org/https://doi.org/10.1029/97JD00237
885	Mohr KI (2004) Interannual, monthly, and regional variability in the Wet season diurnal cycle of
886	precipitation in sub-Saharan Africa. J Clim 17:2441–2453. https://doi.org/10.1175/1520-
887	0442(2004)017<2441:IMARVI>2.0.CO;2

888	Mulholland JP, Peters JM, Morrison H (2021) How Does Vertical Wind Shear Influence
889	Entrainment in Squall Lines? J Atmos Sci 78:1931–1946.
890	https://doi.org/https://doi.org/10.1175/JAS-D-20-0299.1
891	Mwanthi A, Mutemi J, Dyer E, et al (2022) Representation of Land-Atmosphere Coupling
892	Processes Over Africa in CMIP6 Models. ResearchSquare 1–22.
893	https://doi.org/10.21203/rs.3.rs-1139508
894	Neelin JD, Martinez-Villalobos C, Stechmann SN, et al (2022) Precipitation Extremes and Water
895	Vapor: Relationships in Current Climate and Implications for Climate Change. Curr Clim
896	Change Rep 8:17–33
897	O'Neill BC, Tebaldi C, van Vuuren DP, et al (2016) The Scenario Model Intercomparison
898	Project (ScenarioMIP) for CMIP6. Geosci Model Dev 9:3461-3482.
899	https://doi.org/10.5194/gmd-9-3461-2016
900	Panthou G, Lebel T, Vischel T, et al (2018) Rainfall intensification in tropical semi-arid regions:
901	The Sahelian case. Environmental Research Letters 13:. https://doi.org/10.1088/1748-
902	9326/aac334
903	Patricola CM, Cook KH (2011) Sub-Saharan Northern African climate at the end of the twenty-
904	first century: forcing factors and climate change processes. Clim Dyn 37:1165–1188.
905	https://doi.org/10.1007/s00382-010-0907-y
906	Patricola CM, Cook KH (2013a) Mid-twenty-first century climate change in the Central United
907	States. Part II: Climate change processes. Clim Dyn 40:569–583.
908	https://doi.org/10.1007/s00382-012-1379-z

909	Patricola CM, Cook KH (2010) Northern African climate at the end of the twenty-first century:
910	an integrated application of regional and global climate models. Clim Dyn 35:193-212.
911	https://doi.org/10.1007/s00382-009-0623-7
912	Patricola CM, Cook KH (2013b) Mid-twenty-first century warm season climate change in the
913	Central United States. Part I: regional and global model predictions. Clim Dyn 40:551-568
914	https://doi.org/10.1007/s00382-012-1605-8
915	Pfahl S, O'Gorman PA, Fischer EM (2017) Understanding the regional pattern of projected
916	future changes in extreme precipitation. Nat Clim Chang 7:423-427.
917	https://doi.org/10.1038/nclimate3287
918	Prein AF, Langhans W, Fosser G, et al (2015) A review on regional convection-permitting
919	climate modeling: Demonstrations, prospects, and challenges. Reviews of Geophysics
920	53:323–361. https://doi.org/10.1002/2014RG000475
921	Quenum GMLD, Nkrumah F, Klutse NAB, Sylla MB (2021) Spatiotemporal changes in
922	temperature and precipitation in West Africa. Part i: Analysis with the CMIP6 historical
923	dataset. Water (Switzerland) 13:. https://doi.org/10.3390/w13243506
924	Roehrig R, Bouniol D, Guichard F, et al (2013) The present and future of the west african
925	monsoon: A process-oriented assessment of CMIP5 simulations along the AMMA transect.
926	J Clim 26:6471–6505. https://doi.org/10.1175/JCLI-D-12-00505.1
927	Rossow WB, Mekonnen A, Pearl C, Goncalves W (2013) Tropical precipitation extremes. J
928	Clim 26:1457–1466. https://doi.org/10.1175/JCLI-D-11-00725.1
929	Rotunno R, Klemp JB, Weisman ML (1988) A Theory for Strong, Long-Lived Squall Lines. J
930	Atmos Sci 45:463–485. https://doi.org/10.1175/1520-
931	0469(1988)045<0463:ATFSLL>2.0.CO;2

932	Semmler T, Danilov S, Rackow T, et al (2018) AWI AWI-CM1.1MR model output prepared for
933	CMIP6 CMIP. Earth System Grid Federation. https://doi.org/10.22033/ESGF/CMIP6.359
934	Seneviratne SI, Zhang X, Adnan M, et al (2021) Weather and Climate Extreme Events in a
935	Changing Climate. In Climate Change 2021: The Physical Science Basis. Contribution of
936	Working Group I to the Sixth Assessment Report of the Intergovernmental Panel on
937	Climate Change [Masson-Delmotte, V., P. Zhai, A. Pirani, S.L. Connors, C. Péan, S.
938	Berger, N. Caud, Y. Chen, L. Goldfarb, M.I. Gomis, M. Huang, K. Leitzell, E. Lonnoy,
939	J.B.R. Matthews, T.K. Maycock, T. Waterfield, O. Yelekçi, R. Yu, and B. Zhou (eds.)].
940	Cambridge, United Kingdom and New York, NY, USA
941	Shepherd TG (2014) Atmospheric circulation as a source of uncertainty in climate change
942	projections. Nat Geosci 7:703–708
943	Skamarock W, Klemp J, Dudhia J, et al (2019) A Description of the Advanced Research WRF
944	Model Version 4.1 (No. NCAR/TN- 556+STR). https://doi.org/doi:10.5065/1dfh-6p97
945	Skinner CB, Diffenbaugh NS (2014) Projected changes in African easterly wave intensity and
946	track in response to greenhouse forcing. Proceedings of the National Academy of Sciences
947	111:6882–6887. https://doi.org/10.1073/pnas.1319597111
948	Stensrud DJ, Coniglio MC, Davies-Jones RP, Evans JS (2005) NOTES AND
949	CORRESPONDENCE Comments on "A Theory for Strong Long-Lived Squall Lines'
950	Revisited"
951	Sugiyama M, Shiogama H, Emori S (2010) Precipitation extreme changes exceeding moisture
952	content increases in MIROC and IPCC climate models. Proceedings of the National
953	Academy of Sciences 107:571-575. https://doi.org/10.1073/pnas.0903186107

954	Sun Q, Zhang X, Zwiers F, et al (2021) A Global, Continental, and Regional Analysis of
955	Changes in Extreme Precipitation. J Clim 34:243–258. https://doi.org/10.1175/JCLI-D-19-
956	0892.1
957	Takemi T (2014) Convection and precipitation under various stability and shear conditions:
958	Squall lines in tropical versus midlatitude environment. Atmos Res 142:111–123.
959	https://doi.org/10.1016/j.atmosres.2013.07.010
960	Takemi T (2007a) A sensitivity of squall-line intensity to environmental static stability under
961	various shear and moisture conditions. Atmos Res 84:374–389.
962	https://doi.org/10.1016/j.atmosres.2006.10.001
963	Takemi T (2006) Impacts of moisture profile on the evolution and organization of midlatitude
964	squall lines under various shear conditions. Atmos Res 82:37-54.
965	https://doi.org/https://doi.org/10.1016/j.atmosres.2005.01.007
966	Takemi T (2007b) Environmental stability control of the intensity of squall lines under low-level
967	shear conditions. Journal of Geophysical Research: Atmospheres 112:.
968	https://doi.org/https://doi.org/10.1029/2007JD008793
969	Taylor CM, Belusic D, Guichard F, et al (2017) Frequency of extreme Sahelian storms tripled
970	since 1982 in satellite observations. Nature 544:475–478.
971	https://doi.org/10.1038/nature22069
972	Taylor CM, Prigent C, Dadson SJ (2018) Mesoscale rainfall patterns observed around wetlands
973	in sub-Saharan Africa. Quarterly Journal of the Royal Meteorological Society 144:2118-
974	2132. https://doi.org/10.1002/qj.3311
975	Thompson G, Field PR, Rasmussen RM, Hall WD (2008) Explicit Forecasts of Winter
976	Precipitation Using an Improved Bulk Microphysics Scheme. Part II: Implementation of a

) 77	New Snow Parameterization. Mon Weather Rev 136:5095–5115.
978	https://doi.org/10.1175/2008MWR2387.1
979	Tian Y, Peters-Lidard CD (2007) Systematic anomalies over inland water bodies in satellite-
980	based precipitation estimates. Geophys Res Lett 34:.
981	https://doi.org/https://doi.org/10.1029/2007GL030787
982	Trenberth KE, Dai A, Rasmussen RM, Parsons DB (2003) The Changing Character of
983	Precipitation. Bull Am Meteorol Soc 84:1205–1218.
984	https://doi.org/https://doi.org/10.1175/BAMS-84-9-1205
985	Trenberth KE, Fasullo JT, Shepherd TG (2015) Attribution of climate extreme events. Nat Clim
986	Chang 5:725–730
987	Vizy EK, Cook KH (2017) Seasonality of the Observed Amplified Sahara Warming Trend and
988	Implications for Sahel Rainfall. J Clim 30:3073-3094. https://doi.org/10.1175/JCLI-D-16-
989	0687.1
990	Vizy EK, Cook KH (2018) Mesoscale convective systems and nocturnal rainfall over the West
991	African Sahel: role of the Inter-tropical front. Clim Dyn 50:587-614.
992	https://doi.org/10.1007/s00382-017-3628-7
993	Vizy EK, Cook KH (2019) Understanding the summertime diurnal cycle of precipitation over
994	sub-Saharan West Africa: regions with daytime rainfall peaks in the absence of significant
995	topographic features. Clim Dyn 52:2903–2922. https://doi.org/10.1007/s00382-018-4315-z
996	Vizy EK, Cook KH (2023) West African Sahel Extreme rainfall events: Understanding storm
997	development over the Damergou Gap using WRF convection-permitting simulations.
998	Quarterly Journal of the Royal Meteorological Society n/a:
999	https://doi.org/https://doi.org/10.1002/qj.4443

1000	Vizy EK, Cook KH (2022) Distribution of extreme rainfall events and their environmental
1001	controls in the West African Sahel and Soudan. Clim Dyn 59:997-1026.
1002	https://doi.org/10.1007/s00382-022-06171-x
1003	Vizy EK, Cook KH (2009) Tropical storm development from African easterly waves in the
1004	Eastern Atlantic: A comparison of two successive waves using a regional model as part of
1005	NASA AMMA 2006. J Atmos Sci 66:3313–3334. https://doi.org/10.1175/2009JAS3064.1
1006	Vizy EK, Cook KH (2012) Mid-Twenty-First-Century Changes in Extreme Events over
1007	Northern and Tropical Africa. J Clim 25:5748–5767.
1008	https://doi.org/https://doi.org/10.1175/JCLI-D-11-00693.1
1009	Vizy EK, Cook KH, Crétat J, Neupane N (2013) Projections of a wetter sahel in the twenty-first
1010	century from global and regional models. J Clim 26:4664-4687.
1011	https://doi.org/10.1175/JCLI-D-12-00533.1
1012	Voldoire A (2019) CNRM-CERFACS CNRM-CM6-1-HR model output prepared for CMIP6
1013	HighResMIP. Earth System Grid Federation. https://doi.org/10.22033/ESGF/CMIP6.1387
1014	von Storch J-S, Putrasahan D, Lohmann K, et al (2017) MPI-M MPIESM1.2-HR model output
1015	prepared for CMIP6 HighResMIP. Earth System Grid Federation.
1016	https://doi.org/10.22033/ESGF/CMIP6.762
1017	Wang C, Prinn RG (1998) Impact of the horizontal wind profile on the convective transport of
1018	chemical species. Journal of Geophysical Research: Atmospheres 103:22063-22071.
1019	https://doi.org/https://doi.org/10.1029/98JD01831
1020	Weisman ML, Klemp JB, Rotunno R (1988) Structure and evolution of numerically simulated
1021	squall lines. 45:1990–2013

1022	Weisman ML, Rotunno R (2004) "A Theory for Strong Long-Lived Squall Lines" Revisited. J
1023	Atmos Sci 61:361-382. https://doi.org/10.1175/1520-
1024	0469(2004)061<0361:ATFSLS>2.0.CO;2
1025	Westra S, Alexander L v, Zwiers FW (2013) Global Increasing Trends in Annual Maximum
1026	Daily Precipitation. J Clim 26:3904–3918. https://doi.org/10.1175/JCLI-D-12-00502.1
1027	Zhang G, Cook KH, Vizy EK (2016a) The diurnal cycle of warm season rainfall over West
1028	Africa. Part II: Convection-permitting simulations. J Clim 29:8439–8454.
1029	https://doi.org/10.1175/JCLI-D-15-0875.1
1030	Zhang G, Cook KH, Vizy EK (2016b) The Diurnal Cycle of Warm Season Rainfall over West
1031	Africa. Part I: Observational Analysis. J Clim 29:8423-8437.
1032	https://doi.org/https://doi.org/10.1175/JCLI-D-15-0874.1
1033	Zhang Z, Li G (2022) Uncertainty in the projected changes of Sahel summer rainfall under
1034	global warming in CMIP5 and CMIP6 multi-model ensembles. Clim Dyn 59:3579–3597.
1035	https://doi.org/10.1007/s00382-022-06284-3
1036	Zhao S, Cook KH, Vizy EK (2022) How shrinkage of Lake Chad affects the local climate. Clim
1037	Dyn. https://doi.org/10.1007/s00382-022-06597-3
1038	
1039	Statements and Declarations:
1040	Funding: This work was funded by NSF Award #1929074
1041	Conflict of interest: Not applicable
1042	Availability of data: All datasets analyzed in this study are freely available from their original
1043	sources. Model data available from author on request
1044	Code availability: Not applicable

Table 1 Indices for rainfall accumulation and intensity of selected heavy rainfall events

Symbol	Long Name and Definition
$\mathrm{D}_{\mathrm{total}}$	Duration (hr) of the heavy rainfall event. The start and end of the rainfall event is defined when rainfall intensity at the location (the grid point) of the event is < 10 mm day ⁻¹ for more than 1 hour.
$\mathbf{P}_{\mathrm{total}}$	Total precipitation (mm) over the duration and at the location of the event.
Imean	Mean intensity (mm hr ⁻¹) over the duration and at the location of the event.
I_{peak}	Peak rain rate (mm hr ⁻¹) over the duration and at the location of the event.
$\omega_{ m peak}$	Maximum updraft velocity (Pa s ⁻¹) at the time of the peak rain rate. ω_{peak} is averaged over a $21x21$ -km ² area centered at the location of the event to account for tilting of the storm's updraft. The upward direction is defined as positive.
H_{ω}	Pressure level of the maximum updraft velocity (hPa) at the time of the peak rain rate over the 21x21-km ² area centered at the location of the event.
$ m A_{peak}$	Area of the storm's 10 mm day ⁻¹ rain shield (km ²) at the time of the peak rain rate. A_{peak} is identified within a ~15° latitude x 20° longitude sub-region that covers full storm area of each event, including the events near the edge of the analysis region.
$A_{convective}$	Area of the storm's 500 mm day ⁻¹ rain shield (km ²) at the time of the peak rain rate.
$A_{stratiform}$	Area of the storm's 10-100 mm day ⁻¹ rain shield (km ²) at the time of the peak rain rate.
$ m V_{peak}$	Storm propagating speed (km hr ⁻¹) at the time of the peak rain rate (t = 0). V_{peak} is calculated as an average of the storm propagating speed at half an hour before and after the peak rain rate of the event, V_{storm} (t = -0.5 hr) and V_{storm} (t = +0.5 hr), which are central differences about the centroid locations of the storm's rain shield at t = -1 hr, t = 0, and t = +1 hr. To reduce the impact of rain-shield deformation on computing the centroid location, the intensity threshold for defining the storm's rain shield is manually selected from 25/50/100/500 mm day ⁻¹ . Specific adjustments are made to the calculation of V_{peak} for 22.1% (12.7%) of the Current-Climate (Future-Warming) events to accommodate the occurrence of large rain-shield deformation, including using different intensity thresholds to derive V_{storm} (t = -0.5 hr) and V_{storm} (t = +0.5 hr), approximating V_{peak} by V_{storm} at t = \pm 0.5 hr, or not calculating V_{peak} for 8 (3) events in Current-Climate (Future-Warming). More information is given in Online Resource 1.

Table 2 Indices for the vertical wind shear and thermodynamic conditions of selected heavy rainfall events. All indices are averaged over the 45x45-km² area centered at the location of the event to represent atmospheric conditions prior to the event, when the mean rainfall intensity over the 45x45-km² area is less than 10 mm day⁻¹

Index Type	Symbol	Long Name and Definition
	du	600 hPa – 925 hPa zonal wind difference (m·s ⁻¹), with the eastward direction defined as positive.
Shear	dv	600 hPa – 925 hPa meridional wind difference (m·s ⁻¹), with the northward direction defined as positive.
	Smagnitude	600 hPa – 925 hPa vertical wind shear speed (m s ⁻¹).
	Sdirection	600 hPa – 925 hPa vertical wind shear direction, measured in degrees (0-360) anti-clockwise from the east.
	q_{800}	800-hPa specific humidity (g kg ⁻¹).
Moisture	q ₆₀₀	600-hPa specific humidity (g kg ⁻¹).
Moisture	q _{gradient}	800 hPa – 600 hPa specific humidity (g kg ⁻¹).
	PW	Precipitable water (mm).
	T ₈₀₀	800-hPa temperature (K).
Temperature	T ₆₀₀	600-hPa temperature (K).
	$T_{gradient}$	800 hPa – 600 hPa temperature (K).
		800 hPa – 600 hPa moist static energy (J kg ⁻¹).
Instability	CAPE ₈₅₀	850-hPa CAPE (J kg ⁻¹).
	CIN ₈₅₀	850-hPa CIN (J kg ⁻¹).

Table 3 Specifications for the initial/lateral boundary/land surface/soil conditions for the Current-Climate and Future-Warming ensemble simulations. Further details on the land surface conditions over Lake Chad are referred to Zhao et al. (2022)

		Future-Warming			
Ensemble Members	5 5		3	3	5
	"Small-Lake"	"Large-Lake"	"Wetland"	"Large-Lake-II"	"Small-Lake"
Land Surface Conditions	A small Lake Chad of 1314 km ² .	A large Lake Chad of 24921 km ² .	A small Lake Chad surrounded by wetlands of 24138 km ² .	A large Lake Chad of 25452 km ² .	A small Lake Chad of 1314 km ² .
Initial/Lateral Boundary Conditions	ERA5 2013-2017	ERA5 2013-2017	ERA5 2013-2015	ERA5 2013-2015	ERA5 2013-2017
Initial Soil Moisture	The 2007 – 2019 average in ERA5 at 00Z 01 July.	The 2007 – 2019 average in ERA5 at 00Z 01 July.	"Small-Lake" 2013 model output at 00Z 01 September.	"Small-Lake" 2013 model output at 00Z 01 September.	The 2007 – 2019 average in ERA5 at 00Z 01 July.

Table 4 CMIP6 models used to derive the anomalies between early and late 21st-century climate. One ensemble member of the SSP585 and historical experiments from each model (i.e., r1i1p1f2 from CNRM-CM6-1-HR and r1i1p1f1 from the other four models) is utilized for computing the anomalies. Near-surface relative humidity is not saved as a monthly mean output variable in AWI-CM-1-1-MR, so the multi-model mean of this variable is calculated based on the other four models. The listed model resolutions are the native nominal resolutions of the atmospheric and oceanic components of the models

Model	Institute	Model Resolution	Reference
GFDL-CM4	NOAA Geophysical Fluid Dynamics Laboratory	Atmos: 100 km Ocean: 25 km	Guo et al. (2018)
EC-Earth3	EC-Earth consortium (EC-Earth)	Atmos: 100 km Ocean: 100 km	EC-Earth (2019)
MPI-ESM1- 2-HR	Max Planck Institute for Meteorology	Atmos: 100 km Ocean: 50 km	von Storch et al. (2017)
AWI-CM-1- 1-MR	Alfred Wegener Institute	Atmos: 100 km Ocean: 25 km	Semmler et al. (2018)
CNRM- CM6-1-HR	Centre National de Recherches Météorologiques	Atmos: 100 km Ocean: 25 km	Voldoire (2019)

Table 5 Correlations between the vertical wind shear indices and the rainfall/storm metrics for the selected heavy rainfall events from the **a** Current-Climate and **b** Future-Warming simulations. The indices represent pre-storm environmental conditions when the mean rainfall intensity over the 45x45-km² area centered at the location of the events is < 10 mm day⁻¹. Pearson correlation coefficients that exceed 90 (95) % confidence level are denoted by * (**), based on two-sided Student's t-tests

(a) Current- Climate	$\omega_{ m peak}$	I _{peak}	H_{ω}	Aconvective	A _{stratiform}	$V_{ m peak}$
du	-0.03	-0.06	-0.14**	-0.28**	-0.19**	-0.46**
dv	0.02	-0.06	-0.08*	-0.15**	-0.05	-0.14**
Smagnitude	0.02	0.07	0.15**	0.29**	0.19**	0.47**
Sdirection	0.00	0.11**	-0.02	0.02	-0.02	-0.06

1	0	6	9
---	---	---	---

(b) Future- Warming	$\omega_{ m peak}$	I _{peak}	H_{ω}	Aconvective	Astratiform	V _{peak}
du	-0.15*	-0.03	-0.05	-0.27**	-0.21**	-0.28**
dv	0.02	0.04	-0.17**	-0.25**	-0.21**	-0.16*
Smagnitude	0.11	0.00	0.08	0.31**	0.25**	0.30**
Sdirection	-0.06	0.00	0.12	0.04	0.04	-0.01

Table 6 Correlations between the thermodynamic indices and the rainfall/storm metrics for the selected heavy rainfall events from the **a** Current-Climate and **b** Future-Warming simulations. The indices represent pre-storm environmental conditions when the mean rainfall intensity over the 45x45-km² area centered at the location of the events is < 10 mm day⁻¹. Pearson correlation coefficients that exceed 90 (95) % confidence level are denoted by * (**), based on two-sided Student's t-tests

 $\begin{array}{c} 1071 \\ 1072 \end{array}$

(a) Current- Climate	$\omega_{ m peak}$	I _{peak}	H_{ω}	Aconvective	A _{stratiform}	$V_{ m peak}$
q ₈₀₀	0.21**	0.10**	-0.15**	0.22**	0.02	0.08
q ₆₀₀	-0.24**	-0.10**	0.01	-0.07	0.02	-0.23**
qgradient	0.30**	0.13**	-0.10**	0.18**	0.00	0.21**
PW	-0.14**	0.02	-0.05	-0.01	0.01	-0.17**
T ₈₀₀	0.08*	0.01	-0.02	0.14**	0.14**	0.36**
T ₆₀₀	-0.11**	0.00	-0.13**	0.00	0.08*	-0.09*
Tgradient	0.12**	0.01	0.04	0.12**	0.08*	0.35**
MSEgradient	0.31**	0.12**	-0.07	0.20**	0.03	0.32**
CAPE ₈₅₀	0.33**	0.19**	-0.13**	0.21**	-0.01	0.27**
CIN ₈₅₀	-0.18**	-0.03	0.15**	0.06	0.12**	0.24**

(b) Future- Warming	$\omega_{ m peak}$	I _{peak}	H_{ω}	Aconvective	Astratiform	V _{peak}
q 800	0.19**	0.17**	-0.05	0.12	-0.13	0.19**
q ₆₀₀	-0.26**	-0.21**	0.04	-0.13	0.02	-0.16**
q _{gradient}	0.27**	0.23**	-0.06	0.15*	-0.09	0.21**
PW	-0.09	-0.02	0.03	0.04	0.00	-0.10
T ₈₀₀	0.33**	0.12	-0.06	0.24**	0.16*	0.44**
T ₆₀₀	-0.04	-0.14*	-0.13	-0.14*	-0.12	-0.17**
Tgradient	0.30**	0.17**	0.00	0.27**	0.19**	0.46**
MSEgradient	0.35**	0.27**	-0.05	0.23**	-0.03	0.35**
CAPE ₈₅₀	0.24**	0.22**	-0.04	0.26**	-0.02	0.32**
CIN ₈₅₀	0.07	-0.14*	0.11	0.18**	0.22**	0.25**

Table 7 Correlations between the vertical wind shear indices and the rainfall/storm metrics for the selected heavy rainfall events from the **a** Current-Climate and **b** Future-Warming simulations. The indices represent environmental conditions 3 hours prior to the peak rain rate of the events. Pearson correlation coefficients that exceed 90 (95) % confidence level are denoted by * (**), based on two-sided Student's t-tests

(a) Current- Climate	$\omega_{ m peak}$	I _{peak}	H_{ω}	Aconvective	A _{stratiform}	V_{peak}
du	-0.09*	-0.11**	-0.11**	-0.23**	-0.12**	-0.46**
dv	0.02	-0.07	-0.09*	-0.14**	-0.04	-0.12**
Smagnitude	0.06	0.09**	0.13**	0.25**	0.13**	0.48**
Sdirection	-0.04	0.04	0	0.04	0.04	-0.06

(b) Future- Warming	$\omega_{ m peak}$	I _{peak}	H_{ω}	Aconvective	$A_{ ext{stratiform}}$	V_{peak}
du	-0.17**	-0.06	-0.08	-0.28**	-0.21**	-0.37**
dv	0.01	0.08	-0.14*	-0.24**	-0.18**	-0.14*
Smagnitude	0.13	0.01	0.12	0.33**	0.25**	0.36**
Sdirection	-0.02	-0.07	0.09	0.04	0.03	-0.04

Table 8 Correlations between the thermodynamic indices and the rainfall/storm metrics for the selected heavy rainfall events from the **a** Current-Climate and **b** Future-Warming simulations. The indices represent environmental conditions 3 hours prior to the peak rain rate of the events. Pearson correlation coefficients that exceed 90 (95) % confidence level are denoted by * (**), based on two-sided Student's t-tests

(a) Current- Climate	$\omega_{ m peak}$	I _{peak}	H_{ω}	Aconvective	Astratiform	$V_{ m peak}$
q 800	0.12**	0.03	-0.15**	0.22**	0.08*	0.05
q ₆₀₀	-0.25**	-0.13**	-0.02	-0.05	0.07	-0.27**
q _{gradient}	0.26**	0.11**	-0.08*	0.17**	-0.01	0.24**
PW	-0.19**	-0.06	-0.05	0	0.08*	-0.22**
T ₈₀₀	0.13**	0.05	-0.02	0.13**	0.1**	0.38**
T ₆₀₀	-0.14**	-0.04	-0.08*	0.03	0.08*	-0.1**
Tgradient	0.18**	0.06	0.02	0.1**	0.04	0.36**
MSEgradient	0.3**	0.12**	-0.06	0.18**	0.01	0.34**
CAPE ₈₅₀	0.31**	0.18**	-0.12**	0.23**	0.01	0.28**
CIN ₈₅₀	-0.11**	-0.02	0.14**	0	0.01	0.21**

(b) Future- Warming	$\omega_{ m peak}$	I _{peak}	H_{ω}	Aconvective	A _{stratiform}	V _{peak}
q 800	0.16*	0.07	-0.08	0.1	-0.12	0.06
q 600	-0.31**	-0.21**	0.07	-0.15*	0.01	-0.24**
q _{gradient}	0.3**	0.18**	-0.09	0.16*	-0.08	0.19**
PW	-0.24**	-0.18**	0.06	-0.06	0	-0.29**
T ₈₀₀	0.39**	0.22**	-0.08	0.27**	0.11	0.52**
T ₆₀₀	0.02	-0.11	-0.11	-0.1	-0.14*	-0.11
Tgradient	0.34**	0.24**	-0.03	0.28**	0.16*	0.51**
MSEgradient	0.38**	0.25**	-0.09	0.23**	-0.02	0.34**
CAPE ₈₅₀	0.28**	0.22**	-0.1	0.26**	-0.05	0.3**
CIN ₈₅₀	0.02	-0.06	0.16*	0.16*	0.17**	0.31**

Table 9 Absolute and relative difference in the vertical wind shear and thermodynamic indices between Current-Climate and Future-Warming simulations for the four groups of events under different shear conditions (Fig. 12). The indices represent pre-storm environmental conditions when the mean rainfall intensity over the 45x45-km² area centered at the location of the events is < 10 mm day⁻¹. Units of the absolute difference in the indices are the same as those listed in Table 1

(a)	1st		2nd			3rd	4th	
du	-0.13	0.58%	-0.42	2.47%	0.17	-1.39%	-0.41	5.21%
dv	-0.45	5.73%	-2.33	46.93%	-0.87	16.38%	-0.85	16.37%
Smagnitude	0.15	0.62%	1.09	5.96%	0.23	1.60%	0.61	6.04%
Sdirection	1.55	0.78%	6.14	3.14%	3.27	1.62%	2.28	1.09%

I	I	U	U
_	_	~	~

(b)	1st		21	nd	3:	rd	4th	
q 800	2.95	22.87%	3.80	29.85%	3.48	27.13%	3.85	30.17%
q ₆₀₀	2.60	51.17%	2.64	52.71%	2.68	53.77%	2.15	39.07%
qgradient	0.35	4.48%	1.16	15.02%	0.80	10.20%	1.69	23.39%
PW	18.40	37.51%	18.44	37.45%	17.85	36.24%	17.65	35.06%
T ₈₀₀	3.65	1.26%	4.07	1.40%	3.71	1.28%	3.88	1.34%
T ₆₀₀	4.62	1.69%	4.31	1.57%	4.36	1.59%	4.23	1.54%
$T_{gradient}$	-0.97	-5.98%	-0.24	-1.54%	-0.65	-4.26%	-0.35	-2.40%
MSEgradient	-497.41	-4.01%	2255.58	19.84%	968.32	8.48%	3503.85	37.92%
CAPE ₈₅₀	137.73	10.71%	580.81	51.35%	324.90	28.94%	646.54	63.90%
CIN ₈₅₀	11.82	51.35%	2.56	17.85%	7.95	76.15%	0.67	9.65%

Table 10 Correlations between the vertical wind shear indices and the thermodynamic metrics for the selected heavy rainfall events from the **a** Current-Climate and **b** Future-Warming simulations. The indices represent pre-storm environmental conditions when the mean rainfall intensity over the 45x45-km² area centered at the location of the events is < 10 mm day⁻¹. Pearson correlation coefficients that exceed 90 (95) % confidence level are denoted by * (**), based on two-sided Student's t-tests

(a) Current-	q ₈₀₀	q ₆₀₀	q _{gradient}	PW	T ₈₀₀	T ₆₀₀	Tgradient	$MSE_{gradient}$	CAPE ₈₅₀	CIN ₈₅₀
Climate										
du	-0.02	0.26**	-0.19**	0.27**	-0.33**	0.24**	-0.39**	-0.32**	-0.21**	-0.31**
dv	0.08*	0.16**	-0.07	0.08*	-0.3**	0.14**	-0.32**	-0.18**	-0.05	-0.39**
Smagnitude	-0.02	-0.26**	0.17**	-0.23**	0.38**	-0.26**	0.45**	0.32**	0.18**	0.42**
Sdirection	-0.02	-0.02	0	0.05	0.08*	0	0.07	0.03	-0.03	0.14**

(b) Future- Warming	q 800	q 600	qgradient	PW	T ₈₀₀	T ₆₀₀	Tgradient	MSEgradient	CAPE ₈₅₀	CIN ₈₅₀
du	0.07	0.07	0	0.1	-0.31**	0.24**	-0.37**	-0.12	-0.06	-0.31**
dv	-0.07	0.09	-0.1	-0.08	-0.24**	0.12	-0.26**	-0.18**	-0.15*	-0.3**
$S_{magnitude}$	-0.02	-0.1	0.04	-0.07	0.35**	-0.25**	0.41**	0.17**	0.11	0.37**
Sdirection	0.09	-0.02	0.07	0.12	0.04	0.06	0.01	0.07	0.06	0.09

Figure Captions

Fig. 1 a Terrain height (m) near the region of analysis ($12^{\circ}N-18^{\circ}N$, $9^{\circ}W-20^{\circ}E$; black rectangle) over the West African Sahel in the 3-km domain. "x" marks the location of an example event from the Current-Climate ensemble simulations. **b** Duration (D_{total} ; hr), total precipitation (P_{total} ; mm), mean intensity (I_{mean} ; mm hr⁻¹), and peak rain rate (I_{peak} ; mm hr⁻¹) at the location of the example event. **c** Precipitation (mm hr⁻¹) at the time of the peak rain rate for the example event. **c** Area of the storm's 10 mm day⁻¹ rain shield (A_{peak} ; km²) at the time of the peak rain rate (t=0) for the example event. **d** Storm propagating speed (V_{peak} ; km hr⁻¹) at the time of the peak rain rate is computed as an average of the storm propagating speed at t = -0.5 hr and t = +0.5 hr that are central differences about the centroid locations of the storm's rain shield at t = -1 hr, t =0, and t = +1 hr. The intensity threshold for defining the rain shield of the example event is 25 mm day⁻¹, manually selected from the 25/50/100/500 mm day⁻¹ thresholds to reduce the impact of rain-shield deformation on computing the centroid location. More information is given in Online Resource 1

Fig. 2 August mean SST anomalies between the Future-Warming and Current-Climate experiments (K; shading) and model configuration for the triple-nested domains. The black, purple, blue, and red rectangles denote the boundaries of the 27-km (10.15°S-33.94°N, 20.63°W-46.63°E), 9-km (5.30°N-29.14°N, 13.24°W-42.23°E), 3-km (1.97°N-27.04°N, 10.53°W-35.03°E) domains, and the analysis region (12°N-18°N, 9°W-20°E), respectively

Fig. 3 a August mean precipitation (mm day⁻¹) averaged over 2000-2019 from IMERG. **b**August mean precipitation (mm day⁻¹) from the 3-km domain of the Current-Climate ensemble

simulations. The rectangles denote the region of analysis (12°N-18°N, 9°W-20°E) over the West African Sahel. c The exceedance probability for 12Z-12Z 24-hr precipitation (mm) at a grid point in the defined analysis region from the IMERG 2000-2019 observations and the Current-Climate ensemble simulations Fig. 4 Spatial distribution of heavy rainfall events (denoted by circles) that produce more than 77 mm precipitation during a 12Z-12Z 24-hr window at one grid point in the analysis region in a IMERG during 2000-2019 and **b** the Current-Climate ensemble simulations. 77 mm is the 99.9th percentile of 24-hr precipitation over the analysis region in the Current-Climate experiment. c Number of heavy rainfall events per August that exceed certain thresholds of 24-hr precipitation (mm) over the analysis region in IMERG and Current-Climate. The thin lines denote data for individual years. The inset shows a closer view of the tails of the curves in c Fig. 5 2000-2019 ERA5 climatological August a 925-hPa and b 600-hPa specific humidity (g kg⁻¹; shading) and horizontal wind (m s⁻¹; vectors). c ERA5 600 hPa – 925 hPa climatological zonal wind (m s⁻¹; shading) and horizontal wind (m s⁻¹; vectors) differences. **d-f** are similar to **a**c, but from the 3-km domain of the Current-Climate ensemble simulations. Vectors exceeding 9 m s⁻¹ are thickened. Vectors are plotted every 8 and 70 grids in **a-c** and **d-f** for clarity, respectively. The rectangles denote the analysis region Fig. 6 a Ensemble mean precipitation (mm day⁻¹) from the Future-Warming simulations. **b** Differences in ensemble mean precipitation (mm day⁻¹) between the Future-Warming and

Current-Climate simulations. The dots denote anomalies that exceed the 95% confidence level

1131

1132

1133

1134

1135

1136

1137

1138

1139

1140

1141

1142

1143

1144

1145

1146

1147

1148

1149

1150

1151

1152

based on a Welch's t-test. The rectangles denote the analysis region. **c** The exceedance probability for 12Z-12Z 24-hr precipitation (mm) at a grid point in the analysis region from the Current-Climate and Future-Warming ensemble simulations

Fig. 7 a Spatial distribution of heavy rainfall events (denoted by circles) that produce 12Z-12Z 24-hr precipitation above 77 mm at one grid point in the analysis region from the Future-Warming ensemble simulations. 77 mm is the 99.9th percentile of 24-hr precipitation over the analysis region in the Current-Climate experiment. **b** Number of heavy rainfall events per August that exceed certain thresholds of 24-hr precipitation (mm) over the analysis region in Current-Climate and Future-Warming. The thin lines denote data for ensemble members. The inset shows a closer view of the tails of the curves in **b**

Fig. 8 a Duration (hr; D_{total}), **b** storm propagation speed at the time of peak rain rate (V_{peak} ; km hr⁻¹), **c** area of the storms' 10 mm day⁻¹ rain shield at the time of peak rain rate (A_{peak} ; 10^4 km²), **d** mean intensity (mm hr⁻¹; I_{mean}), **e** peak rain rate (mm hr⁻¹; I_{peak}), and **f** ratio of rainfall during the hour of the peak rain rate to the total precipitation (P_{peak}/P_{total}) of the selected heavy rainfall events from Current-Climate and Future-Warming. The x-axes show the ranking of the events based on their rainfall totals, P_{total} . For Current-Climate, each dot represents an average of 80 measurements, including 5 events (e.g., $1^{st} - 5^{th}$) per ensemble member multiplied by 16 ensemble members. For Future-Warming, each dot represents an average of 25 measurements (5 events x 5 ensemble members). Error bars denote standard errors of the means. Blue squares denote differences between Future-Warming and Current-Climate that exceed the 95%

confidence level based on Welch's t-tests. Table 1 lists detailed descriptions of the indices for heavy rainfall events

Fig. 9 Differences in the a 925-hPa and b 600-hPa specific humidity (g kg⁻¹; shading) and horizontal wind (m s⁻¹; vectors) between the Future-Warming and Current-Climate ensemble mean. Grey shading masks out differences that do not exceed 95% confidence level based on a Welch's t-test. c Differences in the 600 hPa – 925 hPa zonal (m s⁻¹; shading) and total (m s⁻¹; vectors) vertical wind shear between Future-Warming and Current-Climate ensemble mean. Thickened vectors denote differences that exceed 95% confidence level based on Welch's t-tests. Vectors are plotted every 70 grid points for clarity. The rectangles denote the analysis region

of change of 600 hPa – 925 hPa horizontal wind shear direction (degree hr⁻¹), **b** 925-hPa and 600-hPa zonal wind (m s⁻¹), **c** 800-hPa and 600-hPa specific humidity (g kg⁻¹) and precipitable water (mm), and **d** 800-hPa and 600-hPa temperature (K) averaged over the 45x45-km² area centered at the location of the heavy rainfall event during the passage of the storm (solid lines) and for the dry-day composite (dashed lines) from Current-Climate. **e-h** are similar to **a-d**, but for Future-Warming. The time of the peak rain rate is defined as time 0 and marked by the dots in the time series

Fig. 11 Vertical profiles of **a** zonal wind (m s⁻¹), **b** meridional wind (m s⁻¹), **c** MSE (10⁵ J kg⁻¹), **d** CAPE (J kg⁻¹), and **e** CIN (J kg⁻¹) averaged over the 45x45-km² area centered at the location of the heavy rainfall event for the storm and dry-day composites from Current-Climate. Pre-storm

environmental conditions are calculated when the mean rainfall intensity over the 45x45-km² area centered at the location of the event is < 10 mm day⁻¹. The dry-day composite presents the same hour of the day as the storm composite. **f-j** are similar to **a-e**, but for both Current-Climate and Future-Warming. The dots denote differences between the storm and dry-day composites or Current-Climate and Future-Warming that exceed 95 % confidence level, based on Welch's t-tests

Fig. 12 a 600hPa – 925hPa zonal vertical wind shear (du; m s⁻¹) and vertical wind shear magnitude (S_{magnitude}; m s⁻¹) prior to the selected heavy rainfall events from Current-Climate and Future-Warming. The dashed lines denote the ranges of du that are used to separate the events into four groups of similar shear strength. The number of events in each group is marked in the figure. b Relative difference (%) in the peak rain rate, I_{peak}, 800-hPa specific humidity, q₈₀₀, precipitable water, PW, and MSE vertical gradient, MSE_{gradient} between Current-Climate and Future-Warming for the four groups of events. c MSE_{gradient} from Current-Climate (solid line; J kg⁻¹) and absolute difference in MSE_{gradient} (dashed line; J kg⁻¹) and q₈₀₀ (g kg⁻¹) between Current-Climate and Future-Warming for the four groups of events

Online Resource 1 Detailed description of how storm velocity is computed and listings of the selected heavy rainfall events over the analysis region of the West African Sahel from Current-Climate and Future-Warming ensemble simulations

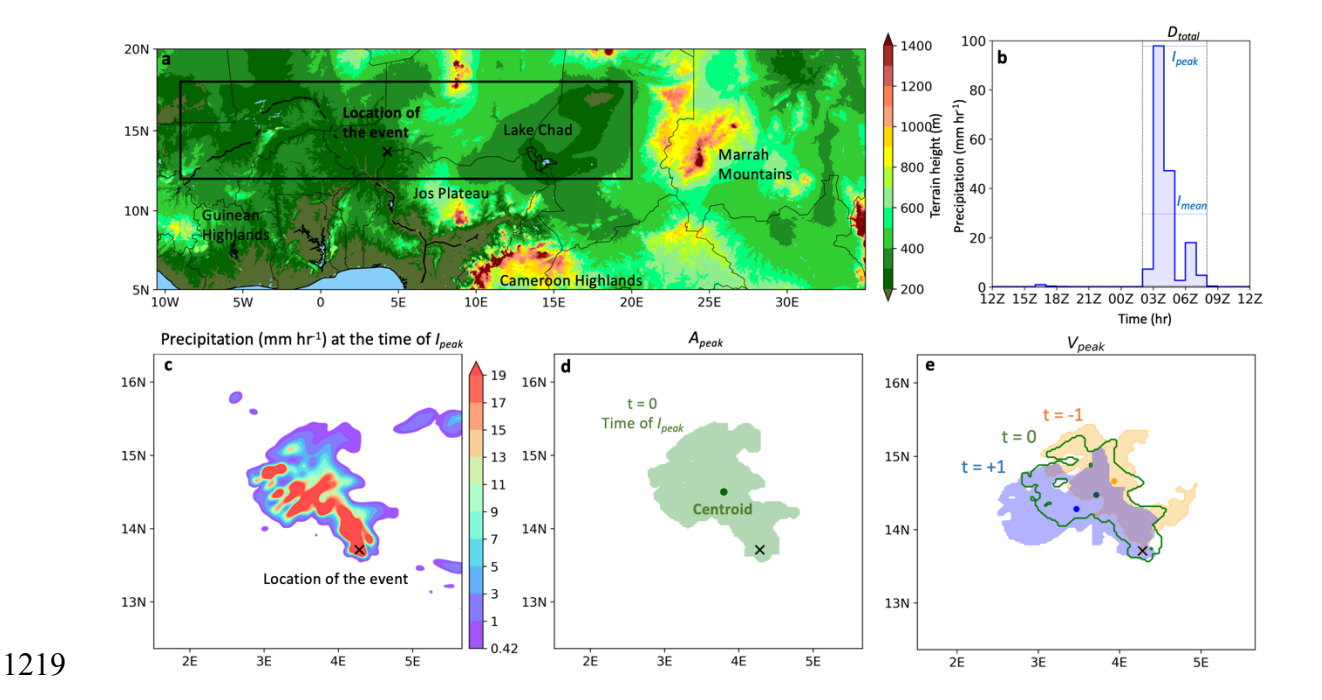


Fig. 1 a Terrain height (m) near the region of analysis (12°N-18°N, 9°W-20°E; black rectangle) over the West African Sahel in the 3-km domain. "x" marks the location of an example event from the Current-Climate ensemble simulations. **b** Duration (D_{total}; hr), total precipitation (P_{total}; mm), mean intensity (I_{mean}; mm hr⁻¹), and peak rain rate (I_{peak}; mm hr⁻¹) at the location of the example event. **c** Precipitation (mm hr⁻¹) at the time of the peak rain rate for the example event. **c** Area of the storm's 10 mm day⁻¹ rain shield (A_{peak}; km²) at the time of the peak rain rate (t=0) for the example event. **d** Storm propagating speed (V_{peak}; km hr⁻¹) at the time of the peak rain rate is computed as an average of the storm propagating speed at t = -0.5 hr and t = +0.5 hr that are central differences about the centroid locations of the storm's rain shield at t = -1 hr, t =0, and t = +1 hr. The intensity threshold for defining the rain shield of the example event is 25 mm day⁻¹, manually selected from the 25/50/100/500 mm day⁻¹ thresholds to reduce the impact of rain-shield deformation on computing the centroid location. More information is given in Online Resource 1

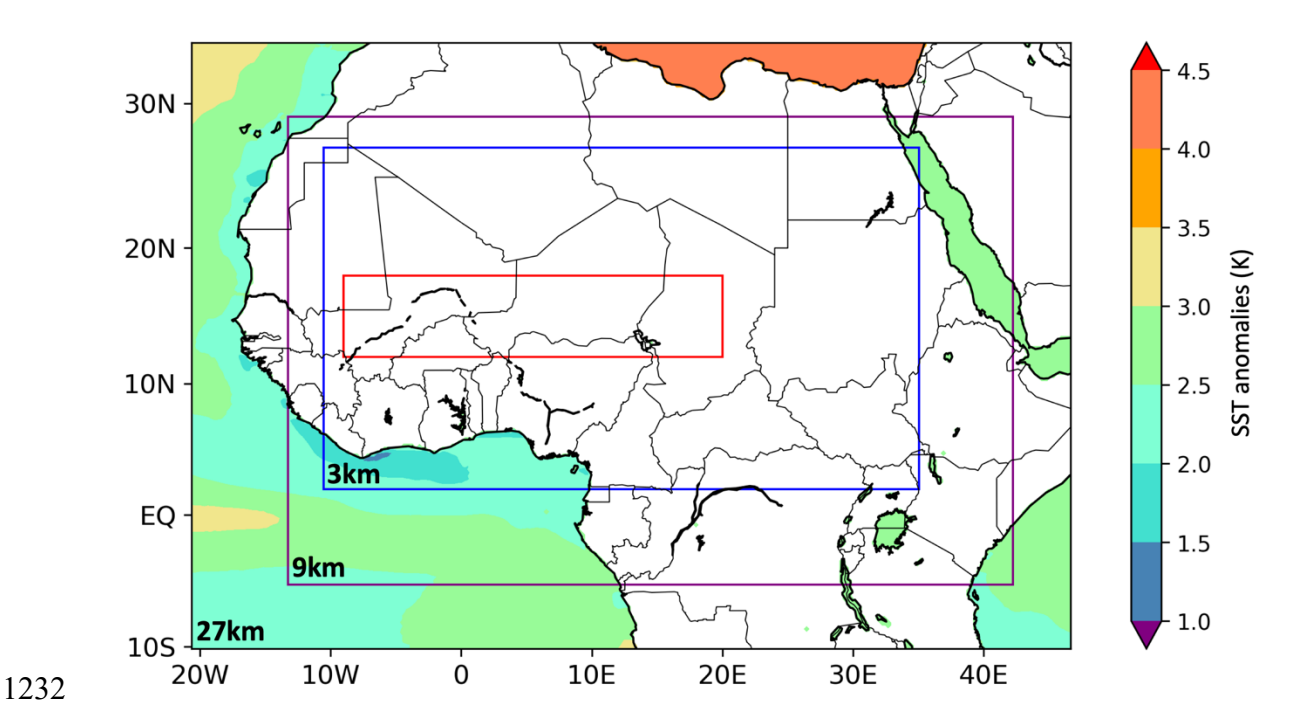


Fig. 2 August mean SST anomalies between the Future-Warming and Current-Climate experiments (K; shading) and model configuration for the triple-nested domains. The black, purple, blue, and red rectangles denote the boundaries of the 27-km (10.15°S-33.94°N, 20.63°W-46.63°E), 9-km (5.30°N-29.14°N, 13.24°W-42.23°E), 3-km (1.97°N-27.04°N, 10.53°W-35.03°E) domains, and the analysis region (12°N-18°N, 9°W-20°E), respectively

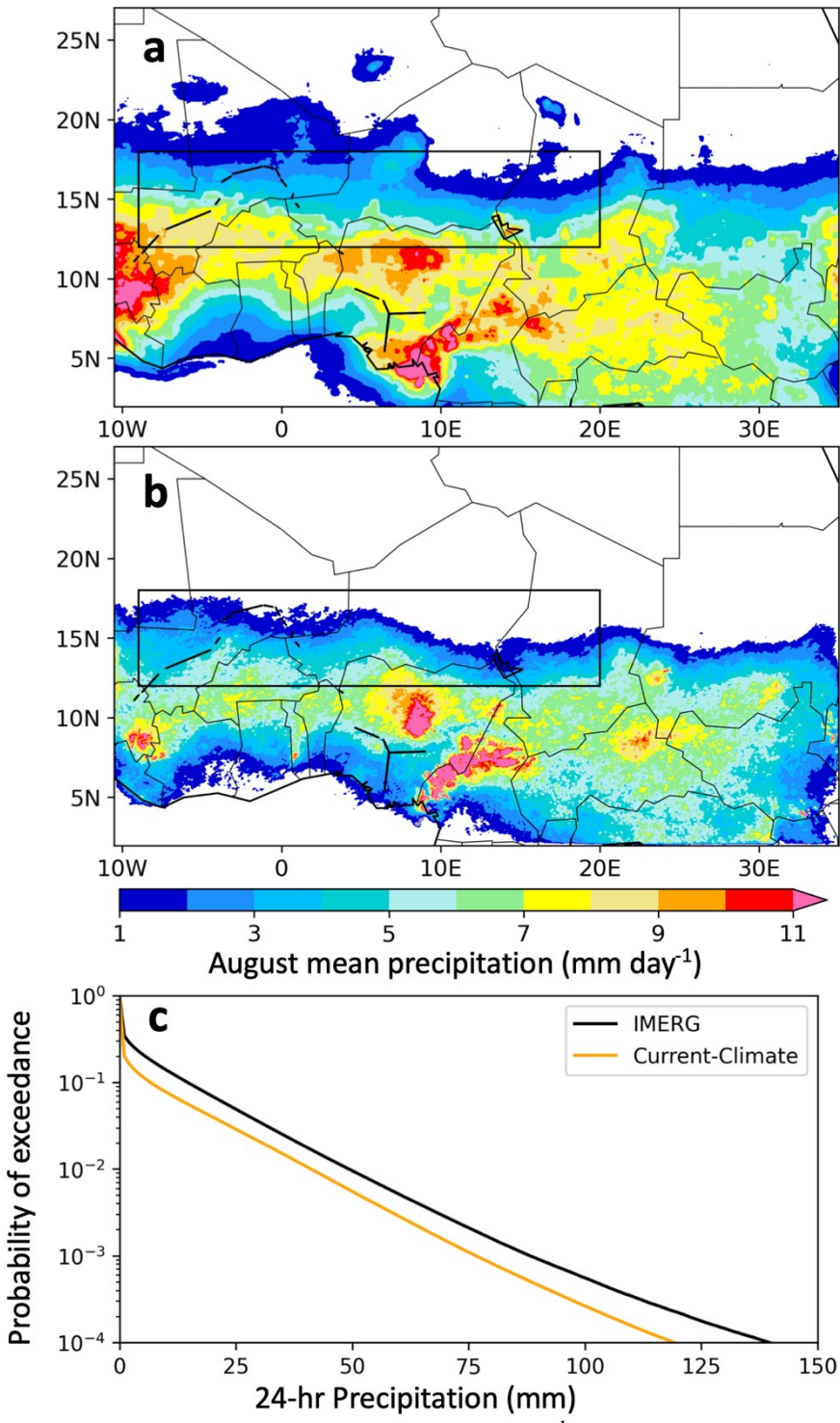


Fig. 3 a August mean precipitation (mm day⁻¹) averaged over 2000-2019 from IMERG. **b** August mean precipitation (mm day⁻¹) from the 3-km domain of the Current-Climate ensemble simulations. The rectangles denote the region of analysis (12°N-18°N, 9°W-20°E) over the West African Sahel. **c** The exceedance probability for 12Z-12Z 24-hr precipitation (mm) at a grid point in the defined analysis region from the IMERG 2000-2019 observations and the Current-Climate ensemble simulations

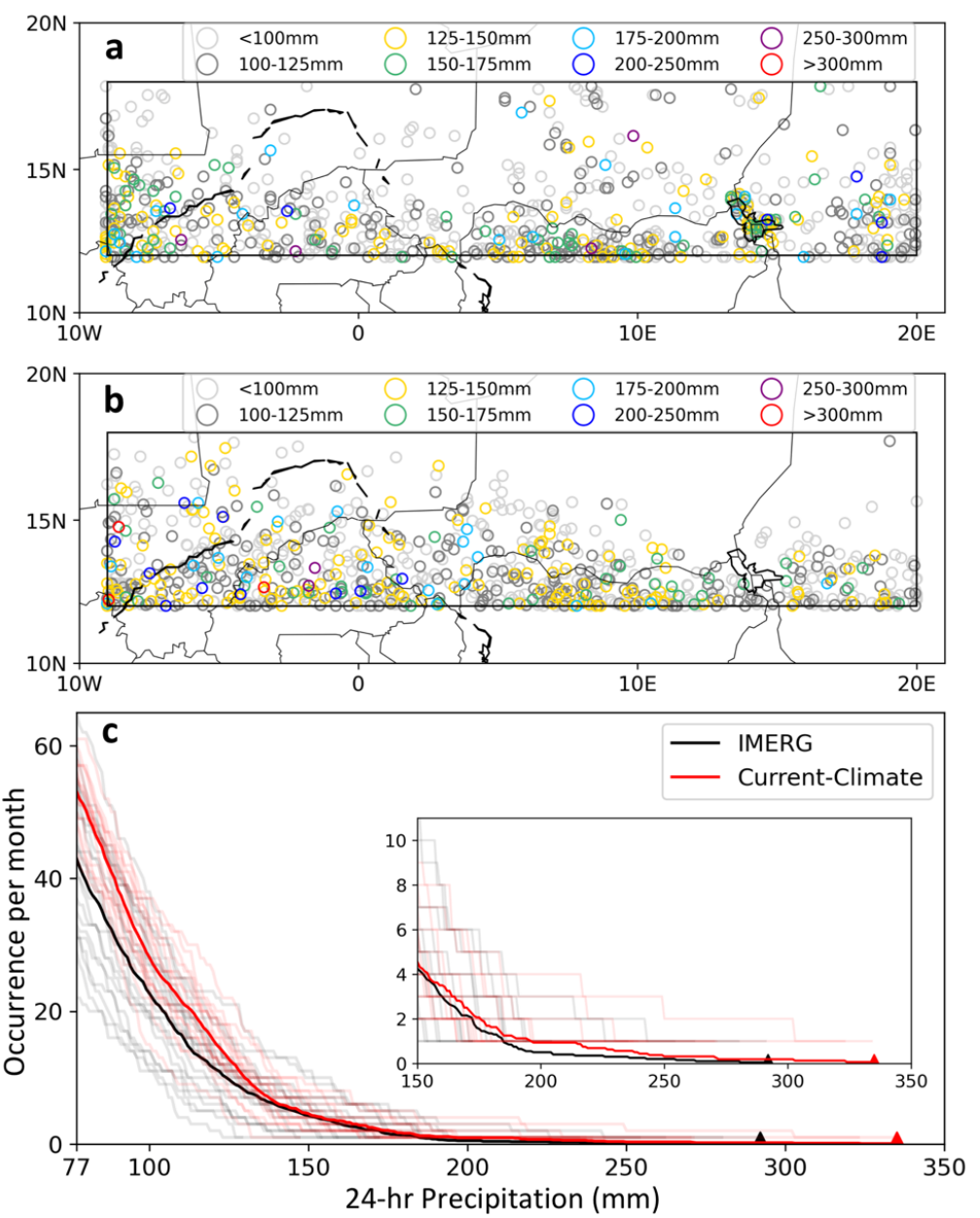


Fig. 4 Spatial distribution of heavy rainfall events (denoted by circles) that produce more than 77 mm precipitation during a 12Z-12Z 24-hr window at one grid point in the analysis region in **a** IMERG during 2000-2019 and **b** the Current-Climate ensemble simulations. 77 mm is the 99.9th percentile of 24-hr precipitation over the analysis region in the Current-Climate experiment. **c** Number of heavy rainfall events per August that exceed certain thresholds of 24-hr precipitation (mm) over the analysis region in IMERG and Current-Climate. The thin lines denote data for individual years. The inset shows a closer view of the tails of the curves in **c**

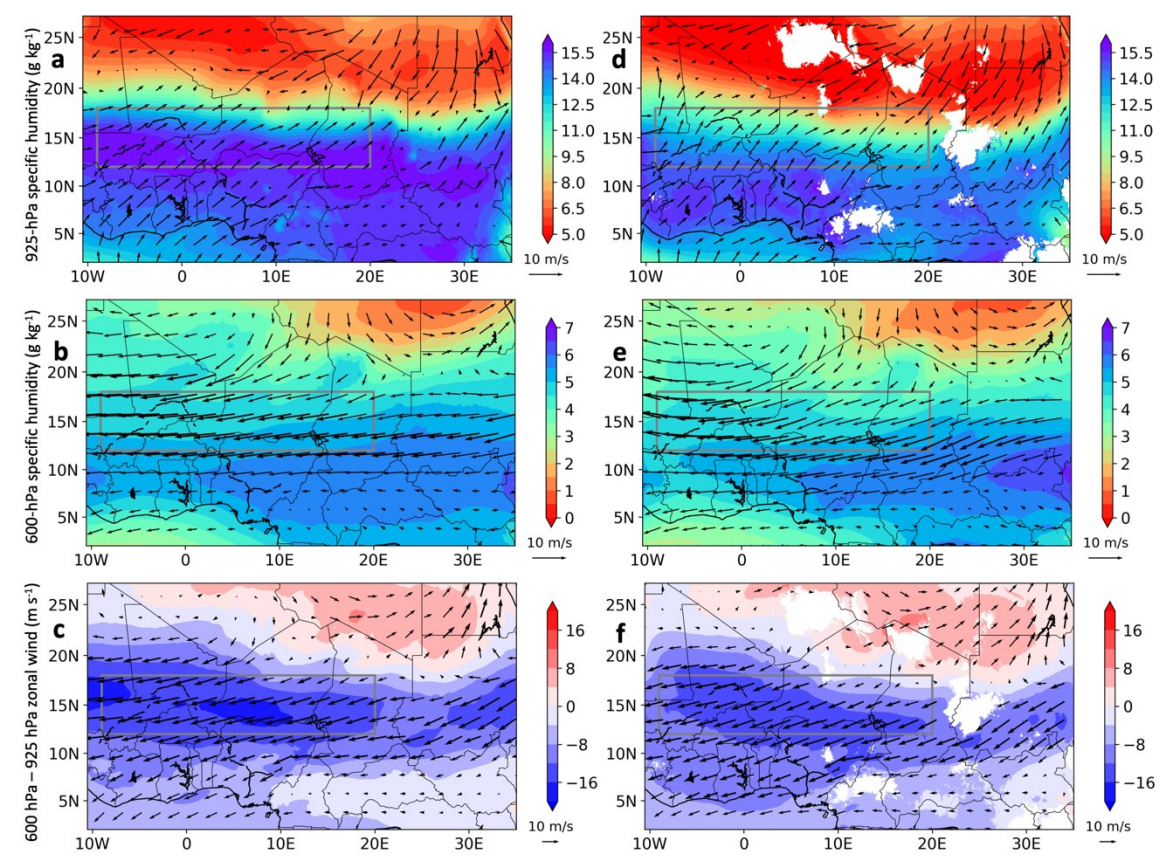


Fig. 5 2000-2019 ERA5 climatological August **a** 925-hPa and **b** 600-hPa specific humidity (g kg⁻¹; shading) and horizontal wind (m s⁻¹; vectors). **c** ERA5 600 hPa – 925 hPa climatological zonal wind (m s⁻¹; shading) and horizontal wind (m s⁻¹; vectors) differences. **d-f** are similar to **a-c**, but from the 3-km domain of the Current-Climate ensemble simulations. Vectors exceeding 9 m s⁻¹ are thickened. Vectors are plotted every 8 and 70 grids in **a-c** and **d-f** for clarity, respectively. The rectangles denote the analysis region

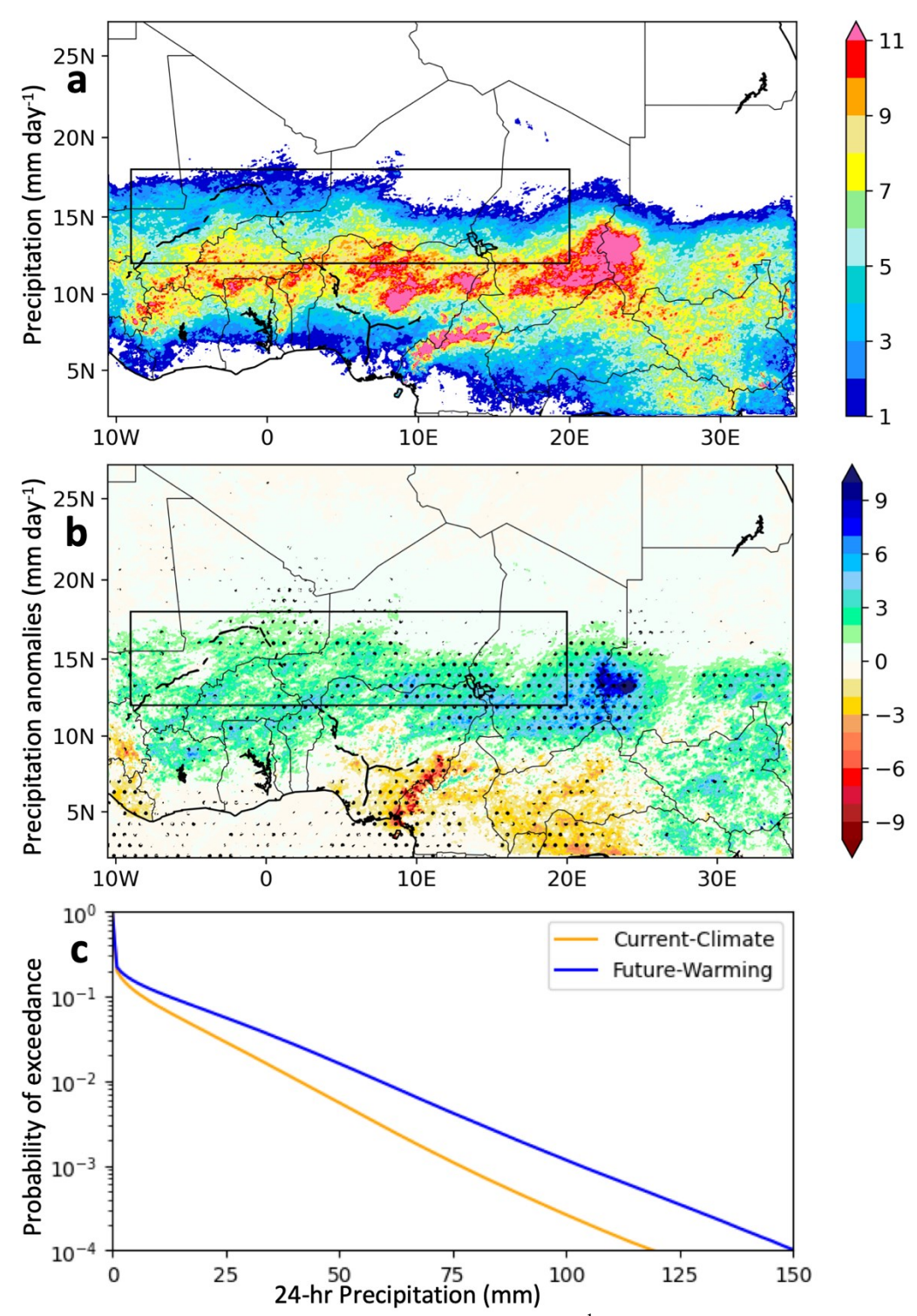


Fig. 6 a Ensemble mean precipitation (mm day⁻¹) from the Future-Warming simulations. **b** Differences in ensemble mean precipitation (mm day⁻¹) between the Future-Warming and Current-Climate simulations. The dots denote anomalies that exceed the 95% confidence level based on a Welch's t-test. The rectangles denote the analysis region. **c** The exceedance probability for 12Z-12Z 24-hr precipitation (mm) at a grid point in the analysis region from the Current-Climate and Future-Warming ensemble simulations

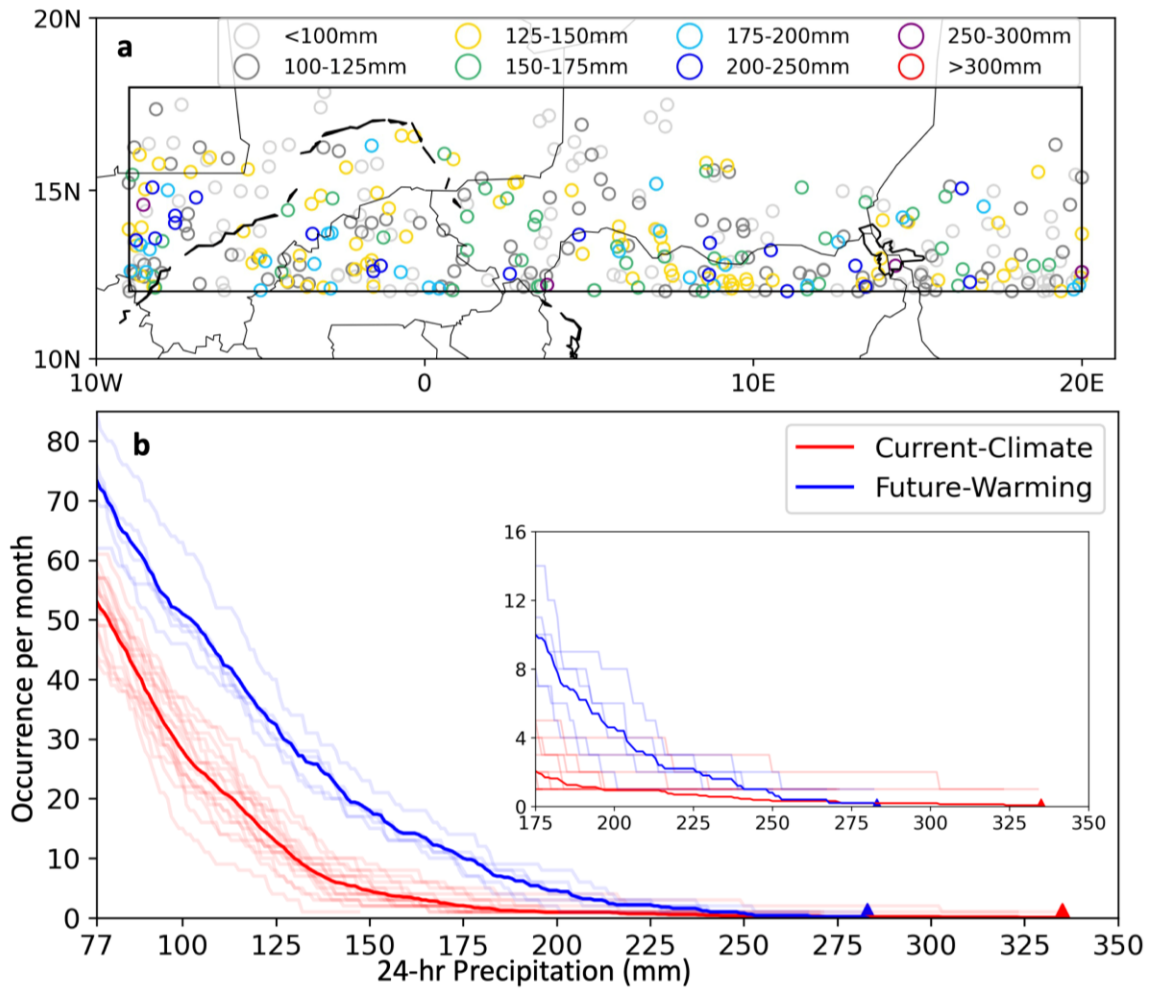


Fig. 7 a Spatial distribution of heavy rainfall events (denoted by circles) that produce 12Z-12Z 24-hr precipitation above 77 mm at one grid point in the analysis region from the Future-Warming ensemble simulations. 77 mm is the 99.9th percentile of 24-hr precipitation over the analysis region in the Current-Climate experiment. **b** Number of heavy rainfall events per August that exceed certain thresholds of 24-hr precipitation (mm) over the analysis region in Current-Climate and Future-Warming. The thin lines denote data for ensemble members. The inset shows a closer view of the tails of the curves in **b**

 $\begin{array}{c} 1272 \\ 1273 \end{array}$

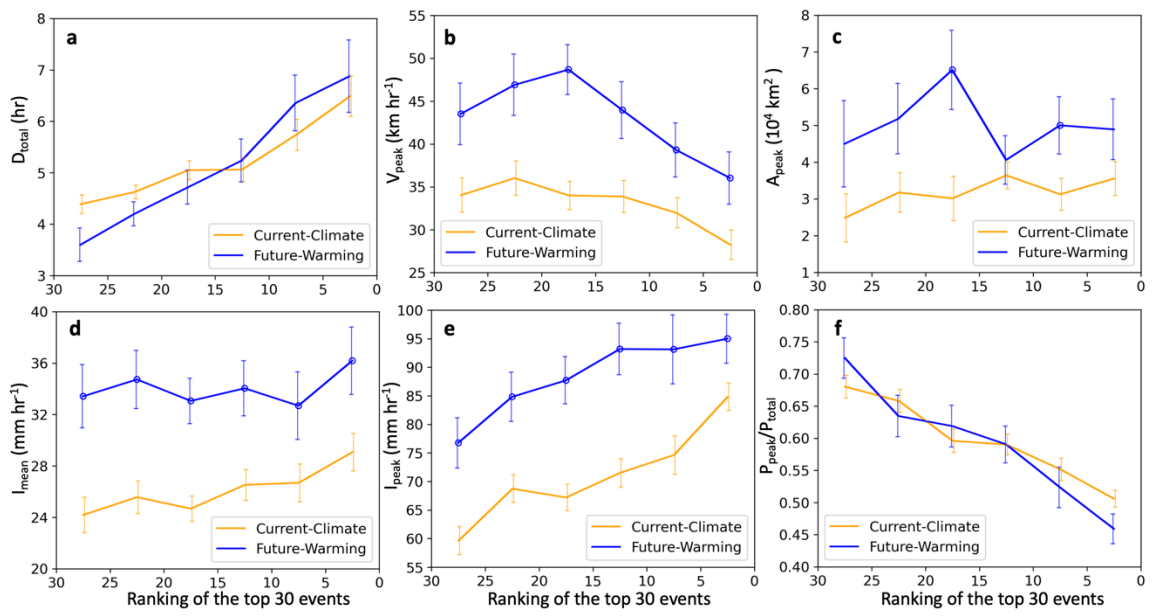


Fig. 8 a Duration (hr; D_{total}), **b** storm propagation speed at the time of peak rain rate (V_{peak} ; km hr⁻¹), **c** area of the storms' 10 mm day⁻¹ rain shield at the time of peak rain rate (A_{peak} ; 10^4 km²), **d** mean intensity (mm hr⁻¹; I_{mean}), **e** peak rain rate (mm hr⁻¹; I_{peak}), and **f** ratio of rainfall during the hour of the peak rain rate to the total precipitation (P_{peak}/P_{total}) of the selected heavy rainfall events from Current-Climate and Future-Warming. The x-axes show the ranking of the events based on their rainfall totals, P_{total} . For Current-Climate, each dot represents an average of 80 measurements, including 5 events (e.g., $1^{st} - 5^{th}$) per ensemble member multiplied by 16 ensemble members. For Future-Warming, each dot represents an average of 25 measurements (5 events x 5 ensemble members). Error bars denote standard errors of the means. Blue circles denote differences between Future-Warming and Current-Climate that exceed the 95% confidence level based on Welch's t-tests. Table 1 lists detailed descriptions of the indices for heavy rainfall events

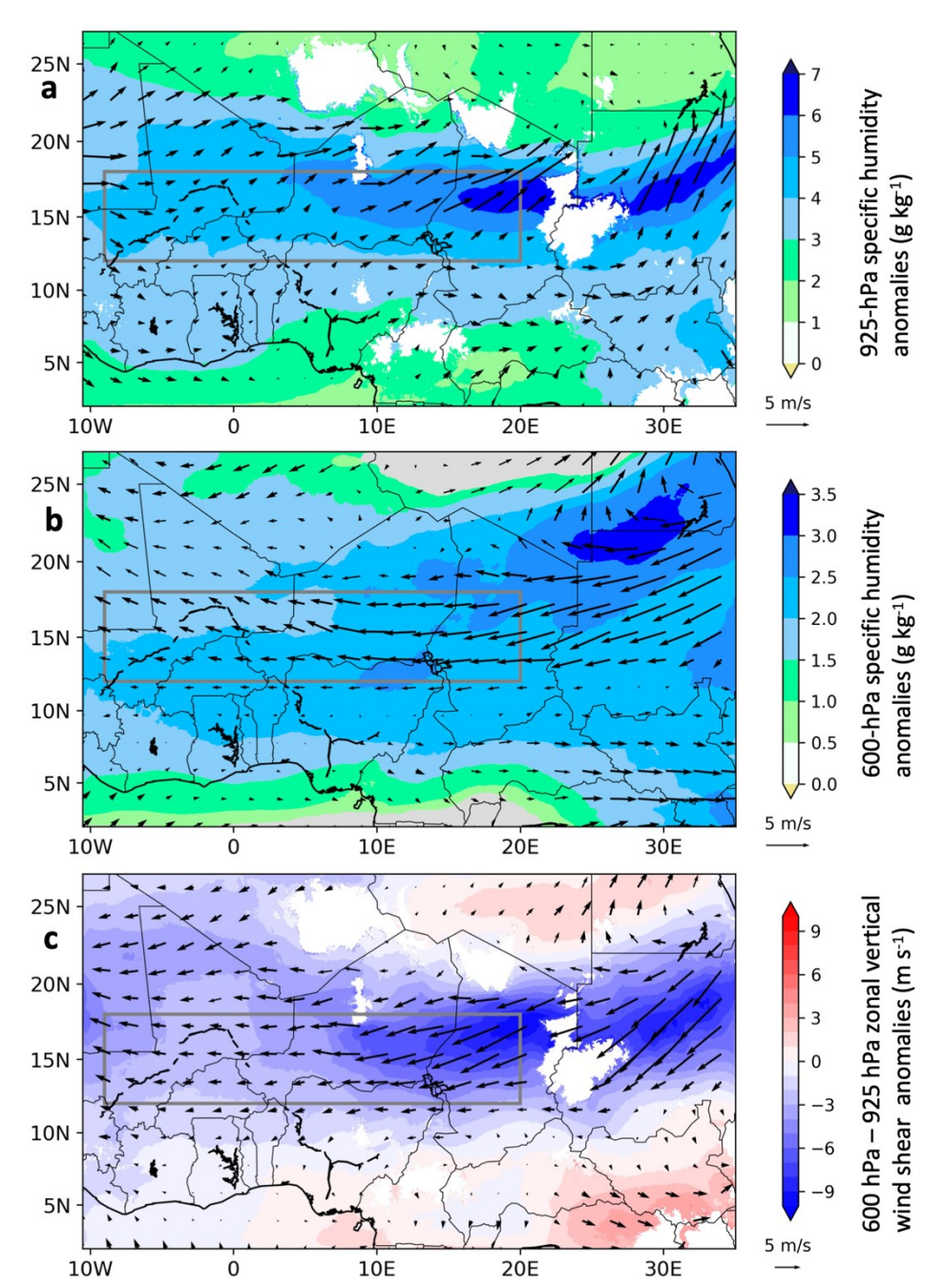


Fig. 9 Differences in the **a** 925-hPa and **b** 600-hPa specific humidity (g kg⁻¹; shading) and horizontal wind (m s⁻¹; vectors) between the Future-Warming and Current-Climate ensemble mean. Grey shading masks out differences that do not exceed 95% confidence level based on a Welch's t-test. **c** Differences in the 600 hPa – 925 hPa zonal (m s⁻¹; shading) and total (m s⁻¹; vectors) vertical wind shear between Future-Warming and Current-Climate ensemble mean. Thickened vectors denote differences that exceed 95% confidence level based on Welch's t-tests. Vectors are plotted every 70 grid points for clarity. The rectangles denote the analysis region

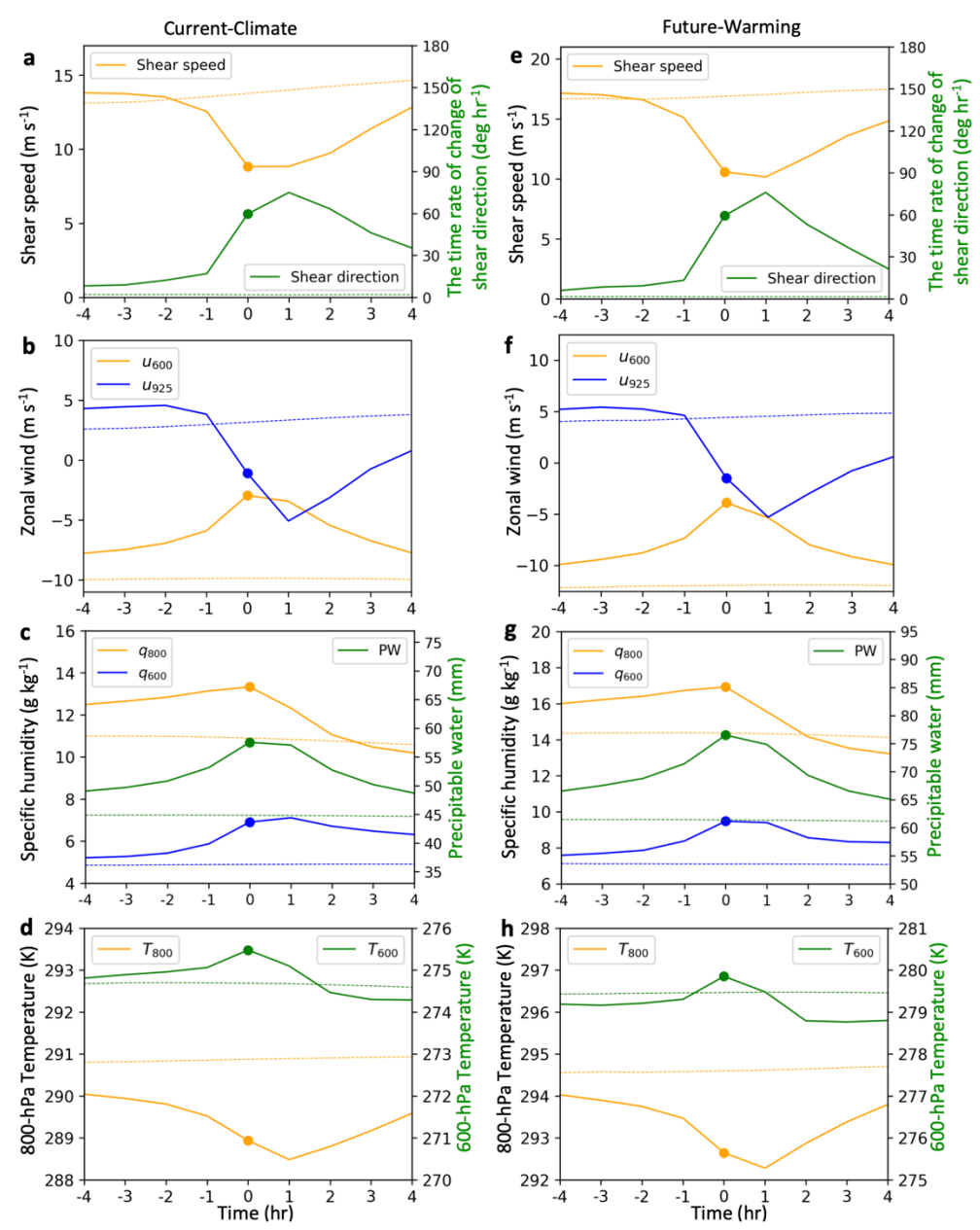


Fig. 10 Time series of **a** 600 hPa – 925 hPa horizontal wind shear speed (m s⁻¹) and the time rate of change of 600 hPa – 925 hPa horizontal wind shear direction (degree hr⁻¹), **b** 925-hPa and 600-hPa zonal wind (m s⁻¹), **c** 800-hPa and 600-hPa specific humidity (g kg⁻¹) and precipitable water (mm), and **d** 800-hPa and 600-hPa temperature (K) averaged over the 45x45-km² area centered at the location of the heavy rainfall event during the passage of the storm (solid lines) and for the dry-day composite (dashed lines) from Current-Climate. **e-h** are similar to **a-d**, but for Future-Warming. The time of the peak rain rate is defined as time 0 and marked by the dots in the time series

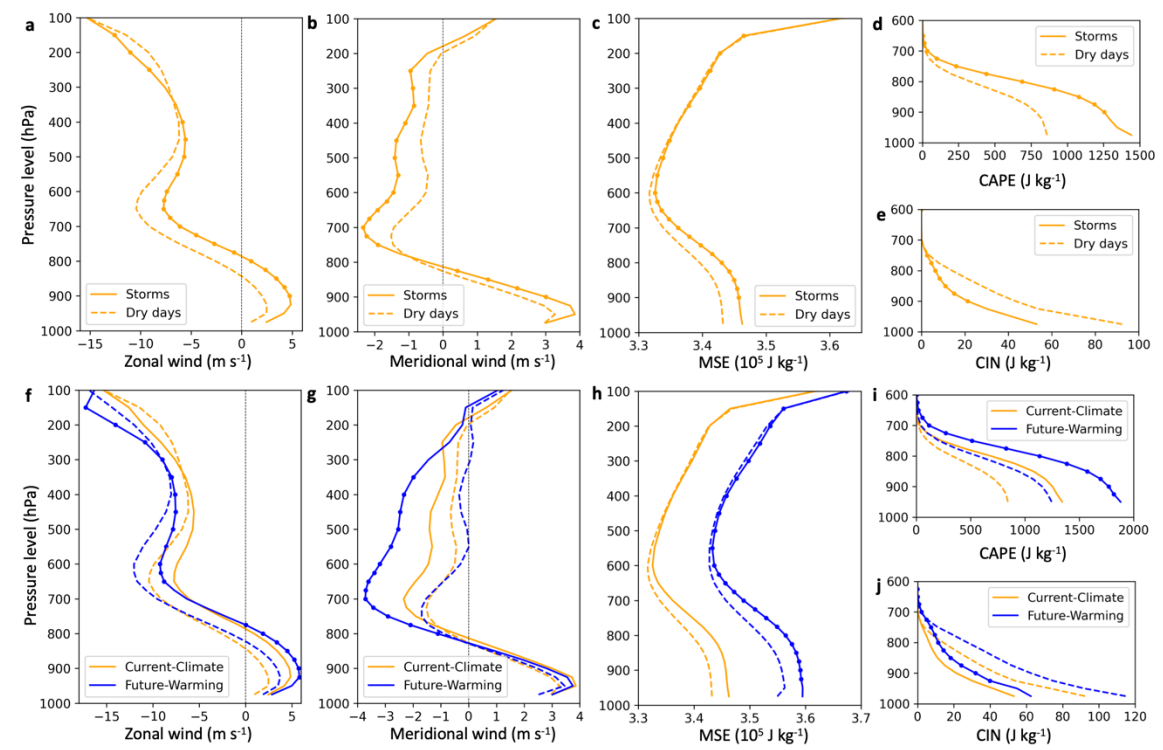


Fig. 11 Vertical profiles of **a** zonal wind (m s⁻¹), **b** meridional wind (m s⁻¹), **c** MSE (10^5 J kg⁻¹), **d** CAPE (J kg⁻¹), and **e** CIN (J kg⁻¹) averaged over the 45x45-km² area centered at the location of the heavy rainfall event for the storm and dry-day composites from Current-Climate. Pre-storm environmental conditions are calculated when the mean rainfall intensity over the 45x45-km² area centered at the location of the event is < 10 mm day⁻¹. The dry-day composite presents the same hour of the day as the storm composite. **f-j** are similar to **a-e**, but for both Current-Climate and Future-Warming. The dots denote differences between the storm and dry-day composites or Current-Climate and Future-Warming that exceed 95 % confidence level, based on Welch's t-tests

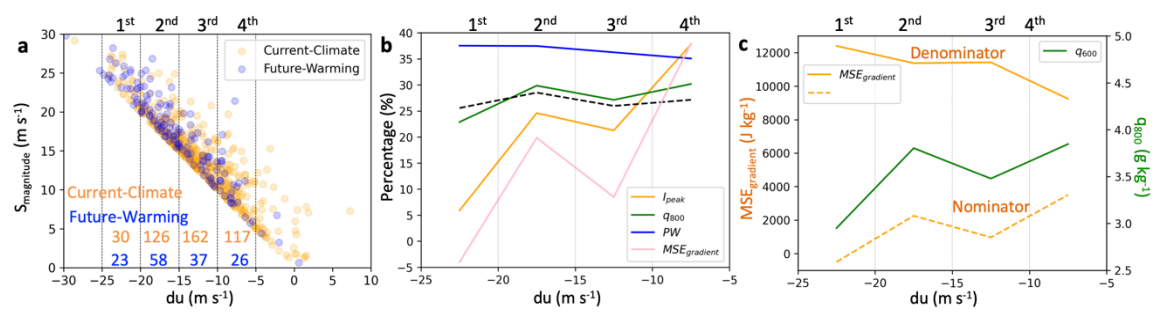


Fig. 12 a 600hPa – 925hPa zonal vertical wind shear (du; m s $^{-1}$) and vertical wind shear magnitude (S_{magnitude}; m s $^{-1}$) prior to the selected heavy rainfall events from Current-Climate and Future-Warming. The dashed lines denote the ranges of du that are used to separate the events into four groups of similar shear strength. The number of events in each group is marked in the figure. **b** Relative difference (%) in the peak rain rate, I_{peak} , 800-hPa specific humidity, q_{800} , precipitable water, PW, and MSE vertical gradient, MSE_{gradient} between Current-Climate and Future-Warming for the four groups of events. **c** MSE_{gradient} from Current-Climate (solid line; J kg $^{-1}$) and absolute difference in MSE_{gradient} (dashed line; J kg $^{-1}$) and q_{800} (g kg $^{-1}$) between Current-Climate and Future-Warming for the four groups of events